# Free convection in drying binary mixtures: solutal versus thermal instabilities.

F. Doumenc[a,*], E. Chénier[b], B. Trouette[b,c], T. Boeck[d], C. Delcarte[c], B. Guerrier[a], M. Rossi[e]

[a] *UPMC Univ Paris 06, Univ Paris-Sud, CNRS, UMR 7608, Lab FAST, Bat 502, Campus Univ.,Orsay F-91405, France*
[b] *Univ Paris-Est, Lab. MSME UMR 8208 CNRS, 5 bd Descartes, Marne-la-vallée, F-77454*
[c] *Univ Paris-Sud, CNRS, LIMSI B.P.133, Orsay, F-91403*
[d] *Institut für Thermo- und Fluiddynamik, Technische Universität Ilmenau, Postfach 100565, 98684 Ilmenau, Germany*
[e] *UPMC Univ Paris 06, CNRS, UMR 7190, IJLRA, 4 place Jussieu, Paris F-75005, France*

**Abstract**

Free convection occuring during the drying of plane layers of polymer solutions may be due to various mechanisms, based on buoyancy or Marangoni effect, of thermal or solutal origin. This theoretical and numerical work provides all the required tools to analyze thoroughly the problem. In this transient flow, different methods (frozen time, non-normal, nonlinear methods) are proposed to predict critical times for convection onset and threshold values for convection. Nonlinear and non-normal methods give similar results, within the uncertainty inherent to any transient problem. It is shown that, when linear stability analysis indicates the presence of several instability mechanisms, it is necessary to invoke nonlinear arguments to establish the leading mechanism. The proposed methodology is then applied to experimental results from the literature for two polymer solutions (Polyisobutylene/toluene and Polystyrene/toluene).

## 1. Introduction

Thermal free convection in a horizontal layer of liquid is still an active field of research since the first experimental studies by H. Bénard a century ago. Driv-

*Corresponding author
*Email address:* doumenc@fast.u-psud.fr (F. Doumenc)

ing forces can originate from density or surface tension dependency on temperature, respectively responsible of buoyancy forces or surface tension gradients. Theoretically, the mechanisms leading to hydrodynamic instabilities have been elucidated first by Rayleigh [33] for the buoyancy-driven flow (Rayleigh-Bénard convection), and by Pearson [31] for the surface-tension-driven flow (Bénard-Marangoni convection). Pearson showed that, for the most common pure liquids, the thermal instability threshold was driven by Marangoni effect for layer thicknesses approximately lower than 1 cm, and by buoyancy for higher thicknesses. Another instability mechanism due to surface deformation can also be present: it is known as the long-wave instability (Scriven and Sternling [41], Reichenbach and Linde [34], Goussis and Kelly [18]). In liquid mixtures, density and surface tension can also depend on concentration. In that case, the above thermal instability mechanisms have also solutal counterparts. For a review of recent developments of Rayleigh-Bénard-Marangoni free convection see Bodenschatz et al. [5], Schatz and Neitzel [39], Colinet et al. [9], Nepomnyashchy et al. [30], Manneville [24].

Free convection induced by evaporation has been studied for a long time, both experimentally and theoretically. In pure liquids or solutions, evaporation at the upper free surface generates a temperature gradient induced by cooling through vaporization latent heat. In the case of solutions, this evaporation also produces a concentration gradient due to difference of components volatility. Both gradients might cause four instability mechanisms at the origin of convective patterns: buoyancy via thermal effects (thermal Rayleigh-Bénard), buoyancy via solutal effects (solutal Rayleigh-Bénard), Marangoni via thermal effects (thermal Bénard-Marangoni) and Marangoni via solutal effects (solutal Bénard-Marangoni). Spangenberg and Rowland [44] used a schlieren technique to characterize the flow pattern driven by thermal buoyancy at the surface of an evaporating thick layer of pure water (10 cm). Berg et al. [4] found a great variety of patterns applying the same technique to several pure substances and solutions of different thicknesses. Certain patterns were induced by buoyancy-driven-instability, and others by surface-tension-driven instability. In the latter

case, these authors demonstrated the importance of surface contamination, very effective for aqueous systems. Indeed, thermal Marangoni convection can hardly be observed in water, because of the high sensitivity of water surface to contamination (Cammenga et al. [7]). More recently, Toussaint et al. [46] and Bassou and Rharbi [2] performed experimental studies of free convection occuring during the drying of polymer solutions. Zhang and co-authors used shadowgraphs techniques to characterize the patterns observed during the drying of NaCl/water solutions (Zhang et al. [57]) and ethanol/water solutions (Zhang et al. [58]).

In these evaporative convection phenomena, which are generally of transient nature, the determination of conditions corresponding to the onset of free convection motivated a lot of works. Some authors performed a linear stability analysis of a one-dimensional steady basic state in a liquid/gas bilayer, when constant temperatures and/or concentrations were prescribed at the bottom and top boundaries (see for instance Merkt and Bestehorn [26], Moussy et al. [29], Machrafi et al. [23]). When the basic state is unsteady as for most of the evaporation processes, various approaches were implemented. The frozen-time approach has been used by Vidal and Acrivos [53] to determine the time of thermal Bénard-Marangoni convection onset in a shallow layer of propyl alcohol. In this approach, one applies a classical normal mode stability analysis to the unsteady basic temperature profile frozen at each given time $t$. The amplification method, which fully takes into account the transient nature of the basic state, was used by Foster [16, 15] to determine the onset time of thermal Rayleigh-Bénard convection in a deep layer of water (10 cm). Good agreement was obtained with experiments for an amplification factor around 10-100. More recently, Doumenc et al. [12] used a non-normal method, which is also based on amplification ideas, to determine the stability conditions of the thermal Rayleigh-Bénard-Marangoni problem in drying polymer solutions. In the thermal problem, Touazi et al. [45] determined the stability threshold using direct nonlinear simulations, and found a good agreement with non-normal results. For the transient solutal problem, nonlinear simulations were also used

by Trouette et al. [48] to pinpoint these thresholds in a configuration with a flat interface and variable viscosity. Serpetsi and Yiantsios [42] also studied the stability of the solutal problem, for a constant viscosity but a deformable interface, using the frozen state approach and nonlinear simulations.

For a given problem, such analysis helps to exhibit the mechanism producing the convection onset. This is particularly interesting for binary mixtures, where many such mechanisms can be potentially active. Pearson [31] extended his famous stability analysis of a pure liquid, to show that a 0.5 mm thick layer of 5 % of ether in liquid paraffin was unstable for the thermal and solutal surface-tension-driven problems, but stable for buoyancy. For the water/ethanol system, Machrafi et al. [23] took into account buoyancy and surface tension effects, of thermal and solutal origin, as well as Soret effect in their linear stability analysis. They concluded that the stability threshold was driven by the solutal Bénard-Marangoni mechanism. In drying polymer solutions, de Gennes [10] used scaling arguments to estimate the critical thickness of the Bénard-Marangoni instability. He concluded that the solutal critical thickness was much smaller than the thermal one, so the concentration effects should dominate the thermal effects. However, drying experiments on polymer solutions performed by Toussaint et al. [46] exhibit experimental results in agreement with thermal Rayleigh-Bénard-Marangoni convection. The reasons of this apparent contradiction are derived in this paper.

The present article focuses on the leading mechanisms and critical conditions for a specific type of evaporative convection: the one occuring in a plane layer geometry and induced by evaporation of a volatile solvent in which a non-volatile solute is diluted. Such a case is of particular interest for coating applications. Indeed, drying of such mixtures (polymer solutions, colloidal suspensions,...) leads to solid-like deposit on the substrate at the end of the process. In some cases, this deposit presents undesirable undulations (self-patterning). Although ruptures of a superficial glassy crust (de Gennes [11]) or buckling of a glassy elastic skin (Huraux et al. [20]) are proposed explanations for these undulations, free convection cells observed during drying are often invoked to understand the non

uniform thickness of the final deposit (Sakurai et al. [38], Weh [54], Sakurai et al. [37], Gorand et al. [17], Bassou and Rharbi [2], Minařík et al. [27], Uchiyama et al. [50, 49], Jun and Lee [21]). For instance, Bassou and Rharbi [2] provides strong experimental evidences connecting solutal Bénard-Marangoni cells and deposit patterning. Apart from this latter work, the convection mechanism (thermal or solutal, surface-tension- or buoyancy-driven) is generally not specified, or it is not supported by clear-cut arguments.

In our previous studies, the thermal problem (Doumenc et al. [12], Touazi et al. [45]) and the solutal problem (Trouette et al. [48]) have been studied independantly. The present work aims at discriminating which is the dominant mechanism for a given set of experimental parameters corresponding to configurations above the thermal and solutal thresholds. When the solutal and the thermal problems are both unstable, it is shown that a stability analysis cannot provide a complete answer. It is then necessary to study the nonlinear regime to decide which mechanism produces the highest velocity in the liquid layer. This article is organized as follows. In section 2, we briefly present the experimental configuration which have been considered to study this transient problem. In section 3, models and dimensionless numbers characterizing the thermal or solutal problems are detailed. Section 4 describes the different methodologies used to derive the conditions leading to convection onset or stability thresholds. In particular, the time and wavelength corresponding to the onset of convection are determined for given non-dimensional numbers. In section 5, comparisons of these results with experiments are presented. First the stability threshold is obtained for both the thermal and the solutal problems. Thereafter, we focus on cases where both thermal and solutal problems are unstable. Critical times, and wavelengths predicted by the thermal and the solutal models are compared with experimental data. In section 6, we focus on the quasi-steady regime in Bénard-Marangoni convection for which we propose a scaling analysis. This provides simple relations for the orders of magnitude of the thermal and solutal velocities in the nonlinear regime. Finally experimental results for the solutal case are compared with the above scaling.

## 2. Experimental Configuration

The typical behavior observed during the drying of a polymer solution is illustrated in figure C.1 for a 8 mm thick plane layer. First, a decrease of the evaporative solvent mass flux per unit area, $Q_m$, is observed ($0 \leq t \lesssim t_1 = 1500$ s). The second stage ($t_1 \lesssim t \lesssim t_2 = 4000$ s) is characterized by a nearly constant evaporative flux (see Trouette et al. [48] for details). In the final regime ($t_2 \lesssim t$), the evaporative flux decreases. First it slowly decreases then it rapidly falls down ($t_3 = 26\ 000$ s $\lesssim t$).

This behavior can be accounted for by using a relationship between $Q_m$ and the saturated vapor pressure $P_{VS}$ of the volatile solvent above the interface. Indeed let us restrict ourselves to the common situation in which evaporation is limited by vapor diffusion in an inert gas, usually air at atmospheric pressure (liquids in contact with their pure vapor can lead to very different behaviors, see for example Uguz and Narayanan [51, 52]). In that case, the phenomenological law (see Guerrier et al. [19])

$$Q_m \;=\; h_m \left[(c_S^g)_{interface} - (c_S^g)_\infty\right] \quad \text{with} \quad (c_S^g)_{interface} = \frac{P_{VS}(T,\varphi_s)\, M_S}{RT} \qquad (1)$$

applies where $(c_S^g)_{interface}$ (resp. $(c_S^g)_\infty$) denotes the solvent vapor concentration in air at the interface (resp. far from the interface). $(c_S^g)_\infty$ is zero in our experiments and $(c_S^g)_{interface}$ is given assuming local thermodynamic equilibrium. $M_S$ stands for the solvent molar mass, $R$ the ideal gas constant. The mass transfer coefficient $h_m$ depends on the air velocity above the solution which is kept constant during all experiments. It is evaluated from measurements obtained from the evaporation kinetics of a pure toluene layer (Toussaint et al. [46], Doumenc et al. [12]).

The dependency of $P_{VS}$ on both temperature $T$ and solvent concentration at the interface $\varphi_s$ explains the succession of several regimes for evaporation flux $Q_m$. The decrease of $Q_m$ for $0 \leq t \lesssim t_1$ is associated to a thermal transient regime in which the cooling induced by evaporation reduces the saturated vapor pressure. The second stage ($t_1 \lesssim t \lesssim t_2$) arises when the temperature of the

solution remains nearly constant and solvent volume fraction $\varphi_s$ remains larger than about 0.4. Indeed the saturated vapor pressure in polymer solution is close to the pure solvent vapor pressure for solvent volume fraction larger than 0.4. This regime is thus characterized by a nearly constant saturated vapor pressure and consequently a nearly constant evaporative flux (see Trouette et al. [48] for details). In the final regime ($t_2 \lesssim t$), the evaporative flux decreases because the saturated vapor pressure of the solution becomes strongly dependent on the solvent concentration.

In this paper, we analyze two sets of experiments: 1) Polyisobutylene (PIB) /toluene solutions performed by Toussaint et al. [46] and 2) Polystyrene (PS) /toluene solutions performed by Bassou and Rharbi [2]. The first set of experiments concerns PIB/toluene films for a fixed evaporation velocity ($v_{ev} \simeq 0.3$ $\mu$m.s$^{-1}$) and a large range of initial thickness $d_i$ and viscosity $\mu_i$ (0.3 mm $\leq d_i \leq$ 24 mm and 0.55 mPa.s $\leq \mu_i \leq$ 2100 mPa.s). Cases 1 and 2 in table 1 correspond to two such instances. Two visualization techniques were used to characterize the onset of convection and the wavelengths of convective patterns and gave identical results. Top views were performed with a Marlin digital camera, the solution being seeded with iriodin particles, or with an IR camera (CEDIP camera, resolution 20 mK). An example of images obtained with the IR camera is given in figure C.2 for the test case 2. Cases 3 to 5 of table 1 correspond to the second sets using thin PS/toluene films (1.4 mm). An important difference between the two sets of experiments concerns the measurement techniques: in thin PS/toluene films, solution velocities were measured by particle tracking, using a microscope. This technique allows the measurement of low velocities, of order of 10 $\mu m.s^{-1}$. Theoretically, we will see that these two sets correspond to two different mechanisms of cells formation.

## 3. Thermal/solutal models

The present paper focuses on the very beginning of drying. Convective cells can be of thermal or solutal origin (see Toussaint et al. [46] or Bassou and Rharbi [2]). To analyze the respective part of these driving mechanisms for convection

| | Case 1 | Case 2 | Case 3 | Case 4 | Case $4^{bis}$ | Case 5 |
|---|---|---|---|---|---|---|
| System | PIB/toluene | PIB/toluene | PS/toluene | PS/toluene | PS/toluene | PS/toluene |
| $d_i(mm)$ | 1 | 8 | 1.4 | 1.4 | 1.4 | 1.4 |
| $\varphi_{pi}$ | 0.006 | 0.047 | 0.1 | 0.15 | 0.15 | 0.2 |
| $\mu_i$ $(mPa.s)$ | 0.98 | 20 | 53 | 185 | 185 | 520 |
| $H_{th}$ $(WK^{-1}m^{-2})$ | 28 | 28 | $\simeq 30$ | $\simeq 30$ | $< 30$ | $\simeq 30$ |
| $\Delta T_{st}$ $(K)$ | 4.8 | 4.8 | $\simeq 5$ | $\simeq 5$ | $< 5$ | $\simeq 5$ |
| $v_{ev}$ $(ms^{-1})$ | $3 \times 10^{-7}$ | $3 \times 10^{-7}$ | $3.5 \times 10^{-7}$ | $3.5 \times 10^{-7}$ | $0.75 \times 10^{-7}$ | $3.5 \times 10^{-7}$ |
| Thermal model | | | | | | |
| $Ma_{th}$ | 6000 | 2400 | 160 | 46 | $< 46$ | 16 |
| $Ra_{th}$ | 460 | 12000 | 25 | 7 | $< 7$ | 3 |
| $Pr$ | 12 | 240 | 620 | 2100 | 2100 | 5900 |
| $Bi$ | 0.20 | 1.6 | 0.30 | 0.30 | $< 0.30$ | 0.30 |
| Solutal model | | | | | | |
| $Ma_{sol}$ | $1.0 \times 10^6$ | $2.4 \times 10^7$ | $6.6 \times 10^5$ | $1.7 \times 10^5$ | $3.7 \times 10^4$ | $6.2 \times 10^4$ |
| $Ra_{sol}$ | $9.2 \times 10^4$ | $1.4 \times 10^8$ | $2.9 \times 10^5$ | $7.6 \times 10^4$ | $1.6 \times 10^4$ | $2.7 \times 10^4$ |
| $Sc$ | $1.1 \times 10^4$ | $2.3 \times 10^5$ | $4.8 \times 10^5$ | $1.3 \times 10^6$ | $1.3 \times 10^6$ | $3.1 \times 10^6$ |
| $Pe_{int}$ | 3.0 | 24 | 3.9 | 3.1 | 0.66 | 2.6 |

Table 1: Experimental configurations with $d_i$ the initial layer thickness, $\varphi_{pi}$ the initial polymer volume fraction, $\mu_i$ the initial solution viscosity, $H_{th}$ the heat transfer coefficient, $\Delta T_{st}$ the characteristic temperature variation, $v_{ev}$ the evaporation velocity. The corresponding dimensionless parameters for both theoretical models are also given (see definitions in sections 3.1 and 3.2). Physical properties of PIB/toluene and PS/toluene solutions are listed in Appendix A. Experiments are performed at room temperature.

onset, we use two separate models: a thermal model and a solutal one. We therefore ignore thermal and solutal coupling effects. This assumption is consistent with our objective, which is the determination of the leading mechanism at short time, just after convection onset. A complete thermo-solutal model would be desirable for a more detailed analysis (like for instance prediction of 3D patterns), or to investigate longer times, when the thermal problem depends on concentration through the viscosity. In addition, Soret effect is supposed to be negligible (this assumption will be justified *a posteriori* by scaling arguments) and we disregard the long-wave instability. This latter mechanism may be pertinent in some experiments (see the numerical simulations by Yiantsios and Higgins [55, 56] for the thermal and solutal problems) but it has not been observed in the experiments presented in section 2.

Both thermal and solutal models share common assumptions: (a) The liquid layer is located between the bottom at $z = 0$ and the upper free surface which remains flat at $z = d(t)$. The layer width $W$ is assumed large with respect

to its height $d(t)$. (b) Bottom and side walls are adiabatic/impermeable, with a no slip condition for velocity. (c) The solution is Newtonian of viscosity $\mu$. Actually non-Newtonian effects are expected in polymer solutions, but only for high enough shear rates, larger than the inverse of the viscoelastic relaxation time of the solution. For test case 2, the shear rate was estimated to be of order of 1 $s^{-1}$. For PIB/toluene at the initial concentration of test case 2 and the same PIB molar mass, no viscoelastic effect were detected in rheometer measurements up to 50 $s^{-1}$ shear rate (Gorand et al. [17]). So viscoelastic effects are unlikely to occur in the beginning of the drying, even if they cannot be excluded at later stage. (d) Liquid density $\rho$ is assumed constant, except in the buoyancy term. (e) Local thermodynamic equilibrium is assumed at the upper evaporative surface. (f) Both models are based on a one-layer approximation in which the heat (mass) transfer in the vapor phase is given by heat (mass) transfer coefficients. (g) For the sake of simplicity, only two-dimensional flows are studied: for the linear problem, the two-dimensional assumption is not a constraint. In addition, 2D and 3D computations gave identical answers on the thermal nonlinear problem (Trouette et al. [47]), when evaluating the orders of magnitude attached to the different processes as performed here.

Since we focus on the beginning of the drying (a few minutes), the liquid height and viscosity variations can be neglected. This assumption has been used in the thermal model. In the solutal model, which has been developped in a previous work to simulate solutal convection over longer times (Trouette et al. [48]), liquid height and viscosity variations are taken into account. For a detailed description of the validity domain of the thermal model, see Doumenc et al. [12], Touazi et al. [45]. The assumptions and the validity domain of the solutal model can be found in Trouette et al. [48].

### *3.1. Thermal model*

The velocity field, $\boldsymbol{v} = v_x \boldsymbol{e_x} + v_z \boldsymbol{e_z}$, is governed by the Navier-Stokes equations in the context of Boussinesq approximation: density $\rho$ is taken to be the

density at $T = T_\infty$ except for the buoyancy term where one sets

$$\rho(T) = \rho(T_\infty)\left[1 - \alpha_{th}\,(T - T_\infty)\right] \tag{2}$$

with $\alpha_{th}$ the thermal expansion coefficient. Surface tension $\sigma(T)$ is a linearly decreasing function of temperature $T$.

$$\sigma(T) = \sigma(T_\infty) - \gamma_{th}\,(T - T_\infty) \tag{3}$$

where $\gamma_{th} > 0$. Finally, the fluid is characterized by a thermal diffusivity $\kappa$. At the upper surface $z = d$, the balance of tangential forces reads

$$\mu\,\frac{\partial v_x}{\partial z} = -\gamma_{th}\frac{\partial T}{\partial x} \qquad \text{at } z = d, \tag{4}$$

and the conservation of energy flux is ensured through the phenomenological equation (for a derivation see Doumenc et al. [12])

$$-\lambda\frac{\partial T}{\partial z} + H_{th}(T_\infty - T(z=d)) = LQ_m(T_\infty), \quad H_{th} = h_{th} + L\frac{\partial Q_m}{\partial T}(T_\infty) \tag{5}$$

where $\lambda$ denotes the thermal conductivity of the liquid, $h_{th}$ the heat transfer coefficient between the gas and the liquid.

The governing equations are put in a dimensionless form using the constant layer thickness $d$, the thermal velocity $V = \kappa/d$ and thermal diffusion time $d/V = d^2/\kappa$ for length, velocity and time scales. Pressure $p$ is scaled by $\kappa\mu/d^2$. Finally one introduces the dimensionless quantity $\theta(x,z,t) = (T(x,z,t) - T_\infty)/\Delta T_{st}$ where

$$\Delta T_{st} \equiv \frac{LQ_m}{H_{th}}. \tag{6}$$

denotes the steady temperature difference in the final steady state regime ($t_1 \lesssim t$). The superscript $*$ is used for dimensionless variables of the thermal model. In Cartesian coordinate system, the equations for dimensionless velocity $\boldsymbol{v}^*$, dimensionless deviation from the hydrostatic pressure $p^*$ and dimensionless temperature $\theta$ read

$$\nabla \cdot \boldsymbol{v}^* = 0, \tag{7}$$

$$\frac{1}{Pr}\left[\frac{\partial \boldsymbol{v}^*}{\partial t^*} + (\boldsymbol{v}^* \cdot \nabla)\boldsymbol{v}^*\right] = -\nabla p^* + \nabla^2 \boldsymbol{v}^* + Ra_{th}\ \theta\ \boldsymbol{e}_z, \tag{8}$$

$$\frac{\partial \theta}{\partial t^*} + (\boldsymbol{v}^* \cdot \nabla)\theta = \nabla^2 \theta, \tag{9}$$

$$\frac{\partial v_x^*}{\partial z^*} + Ma_{th}\,\frac{\partial \theta}{\partial x^*} = 0 \qquad \text{at } z^* = 1. \tag{10}$$

$$\frac{\partial \theta}{\partial z^*} + Bi\,\theta + Bi = 0 \quad \text{at } z^* = 1, \tag{11}$$

$$\frac{\partial \theta}{\partial z^*} = 0 \quad \text{at } z^* = 0, \qquad \frac{\partial \theta}{\partial x^*} = 0 \quad \text{at } x^* = 0, A, \tag{12}$$

$$v_z^* = 0 \ \text{ at } z^* = 1, \qquad v_x^* = v_z^* = 0 \qquad \text{at } z^* = 0 \ \text{ or } x^* = 0, A. \tag{13}$$

This system depends on five dimensionless parameters: Rayleigh, Marangoni, Biot, Prandtl numbers and an aspect ratio

$$Ra_{th} \equiv \frac{\alpha_{th} g \rho d^3 \Delta T_{st}}{\mu\kappa},\ Ma_{th} \equiv \frac{\gamma_{th} d \Delta T_{st}}{\mu\kappa},\ Bi \equiv \frac{H_{th} d}{\lambda},\ Pr \equiv \frac{\mu}{\rho\kappa},\ A \equiv \frac{W}{d}. \tag{14}$$

The analysis is restricted to Prandtl number $Pr \geq 1$. This assumption is clearly valid for most of the liquids, if one excepts liquid metals. It means that the thermal diffusion time scale is always larger than the viscous diffusion time scale. In all the simulations, the aspect ratio is large ($A = 20$ for the thermal problem). It was checked that, when large enough, $A$ does not affect our results.

*3.2. Solutal model*

In the solutal model, the temperature is assumed constant ($T \simeq T_\infty$) and the fluid is a binary solution with a constant diffusion coefficient $D$. The system is characterized by the solvent volume fraction $\varphi_s(x, z, t)$ or the polymer volume fraction $\varphi_p(x, z, t) = 1 - \varphi_s(x, z, t)$. During drying, these concentrations are inhomogeneous and unsteady up to the very end when the film is totally dry ($\varphi_s = 0$).

The velocity field is governed by the Navier-Stokes equations. The difference between pure polymer and pure solvent densities being around 6% for PIB/toluene and 20% for PS/toluene, density $\rho$ is assumed constant and equal to $\rho_i$ the density at the initial solvent volume fraction $\varphi_{si}$, except for the buoyancy term where one sets

$$\rho = \rho_0\,(1 + \alpha_{sol}\ (1 - \varphi_s)) \tag{15}$$

where $\rho_0$ denotes the density of the pure solvent and $\alpha_{sol} > 0$ the solutal expansion coefficient. The interface possesses a surface tension $\sigma$ which is a linear function of $\varphi_s$

$$\sigma = \sigma_0 + \gamma_{sol}\ (1 - \varphi_s), \tag{16}$$

with $\sigma_0$ the surface tension of the pure solvent and $\gamma_{sol} > 0$. By contrast to the thermal model, this model was used previously to study solutal convection over time horizon $t = t_2$, so it takes into account the variation of viscosity $\mu$ with respect to the the polymer volume fraction $\varphi_p$. For the two polymer solutions (PIB/toluene and PS/toluene) used to compare models to experiments, viscosity varies over several orders of magnitude (see figure C.3). This dependency is represented by an empirical law

$$\log_{10}(\mu) = a_0\ +\ a_1\, Y\ +\ a_2\, Y^2\ +\ a_3\, Y^3\ +\ a_4\, Y^4 \tag{17}$$

with $Y = \log_{10}(\varphi_p)$ and $a_i$ are fixed coefficients (for details see Appendix A).

We assume that the evaporative flux remains constant. As mentioned in section 2, this is only approximately valid during the period $t \lesssim t_1$ (typically 30 percent variation due to evaporation induced cooling) and experimentally verified during the period $t_1 \lesssim t \lesssim t_2$. It is thus possible to simulate the drying process up to time $t_2$ when the solvent volume fraction reaches about 0.4 (Trouette et al. [48]) after which the flux is no more steady. The evaporative flux being constant and the surface remaining flat, the layer thickness $d(t) = d(0) - v_{ev}t$ decreases at a constant velocity $v_{ev}$. At the upper surface, the balance of the tangential stresses imposes

$$\mu \frac{\partial v_x}{\partial z} = -\gamma_{sol} \frac{\partial \varphi_s}{\partial x} \quad \text{at } z = d(t) \tag{18}$$

The solvent and polymer mass conservation leads to two additional boundary conditions (see Trouette et al. [48] for a derivation)

$$v_z = 0 \quad \text{at } z = d(t), \tag{19}$$

$$-D \frac{\partial \varphi_s}{\partial z} = v_{ev}(1 - \varphi_s) \quad \text{at } z = d(t), \tag{20}$$

Dimensionless equations are obtained by scaling coordinates $x$ and $z$, velocity $\boldsymbol{v}$, dynamic pressure $p$ and time $t$ respectively by $d_i$, $D/d_i$, $\mu_i D/d_i^2$ and $d_i^2/D$ where $d_i$ is the initial thickness and $\mu_i$ the initial viscosity. Superscripts + are used for dimensionless variables of the solutal model. In addition to $\boldsymbol{v}^+$, $p^+$, one introduces, based on the solvent volume fraction $\varphi$, the quantity

$$\phi_s = \frac{\varphi_s - \varphi_{si}}{\Delta\varphi}$$

where $\varphi_{si}$ is the initial solvent volume fraction and $\Delta\varphi$ is based on the concentration gradient near the interface and the layer thickness

$$\Delta\varphi \equiv -d_i \left.\frac{\partial \varphi_s(z=d_i, t=0)}{\partial z}\right|_{int} = Pe_{int}\ \ (1-\varphi_{si}) \tag{21}$$

where $\varphi_{si}$ is the initial solvent volume fraction and $Pe_{int} \equiv v_{ev} d_i/D$ is a Péclet number based on the interface velocity (Trouette et al. [48]).

This scaling is customary when the evaporation flux is imposed at the boundary. The dimensionless equations for $\boldsymbol{v}^+$, $p^+$ and $\phi_s$ then read

$$\nabla \cdot \boldsymbol{v}^+ = 0, \tag{22}$$

$$\frac{1}{Sc}\left[\frac{\partial \boldsymbol{v}^+}{\partial t^+} + (\boldsymbol{v}^+ \cdot \nabla)\boldsymbol{v}^+\right] = -\nabla p^+ + \nabla \cdot \left(\frac{\mu}{\mu_i}\left(\nabla \boldsymbol{v}^+ + \nabla^T \boldsymbol{v}^+\right)\right) + Ra_{sol}\ \phi_s \boldsymbol{e_z} \tag{23}$$

$$\frac{\partial \phi_s}{\partial t^+} + (\boldsymbol{v}^+ \cdot \nabla)\phi_s = \nabla^2 \phi_s, \tag{24}$$

$$\frac{\partial v_x^+}{\partial z^+} + \frac{\mu_i}{\mu}\, Ma_{sol}\, \frac{\partial \phi_s}{\partial x^+} = 0 \qquad \text{at } z^+ = 1 - Pe_{int} t^+. \tag{25}$$

$$\frac{\partial \phi_s}{\partial z^+} + 1 - Pe_{int}\, \phi_s = 0 \quad \text{at } z^+ = 1 - Pe_{int} t^+, \tag{26}$$

$$\frac{\partial \phi_s}{\partial z^+} = 0 \quad \text{at } z^+ = 0, \qquad \frac{\partial \phi_s}{\partial x^+} = 0 \ \text{ at } x^+ = 0, A, \tag{27}$$

$$v_z^+ = 0, \ \text{ at } z^+ = 1 - Pe_{int} t^+ \qquad v_x^+ = v_z^+ = 0 \quad \text{at } z^+ = 0 \text{ or } x^+ = 0, A. \tag{28}$$

This problem depends on the initial solvent volume fraction $\varphi_{si}$ through the concentration-dependent viscosity $\mu/\mu_i$ (see Eq. (17)), on the Péclet number $Pe_{int}$, as well as on the Rayleigh, Marangoni, Schmidt dimensionless parameters and on the initial aspect ratio $A$

$$Ra_{sol} \equiv \frac{\alpha'_{sol} g \rho d_i^3 \Delta\varphi}{\mu_i D},\ Ma_{sol} \equiv \frac{\gamma_{sol} d_i \Delta\varphi}{\mu_i D},\ Pe_{int} \equiv \frac{v_{ev} d_i}{D},\ Sc \equiv \frac{\mu_i}{\rho_i D},\ A \equiv \frac{W}{d_i} \tag{29}$$

with $\alpha'_{sol} = \alpha_{sol}/[1+\alpha_{sol}\ (1-\varphi_{si})]$. In all simulations, the aspect ratio is large ($5 \leq A \leq 30$ for the solutal problem). It was checked that, when large enough, $A$ does not affect our results.

## 4. Convection Onset and Marginal Stability Determination Methods

The configurations studied are known to display a transition from a purely diffusive state to convective patterns. Since the undisturbed pure diffusive state is unsteady, determination of convection onset amounts at defining a time for convection onset and a corresponding wavenumber. In the subsection below, we present linear and nonlinear methods to determine when does the convection start for a given set of control parameters (14) or (29), and at which wavelength. This leads also to the determination of the marginal stability curve for this unsteady problem.

### *4.1. Time and wavenumber corresponding to Convection Onset: Nonlinear Approach*

This first method necessitates nonlinear two-dimensional simulations to be performed. For both thermal and solutal problems, they are based on finite volume schemes (see Touazi et al. [45] and Trouette et al. [48] for details). In order to take into consideration the moving upper surface in the solutal problem, this numerical method is based on moving grids (Trouette et al. [48]). In both models, the initial velocity field is set to zero. For the thermal problem, the initial dimensionless temperature field $\theta(x^*, z^*, t^* = 0)$ is a random perturbation added at each discretized spatial location. This random perturbation is of zero mean and uniformly distributed between $-r^*/2$ and $r^*/2$ [47, 8]. For the solutal problem, the initial dimensionless solvent volume fraction $\phi_s(x^+, z^+, t^+ = 0)$ is also a similar random field of zero mean and uniformly distributed between $-r^+/2$ and $r^+/2$.

Let us denote by $< q(z_0, t) >$ the mean of quantity $q(x, z_0, t)$ spatially averaged over the horizontal plane $z = z_0$. For the thermal problem, these simulations provide the difference $< T(z = 0, t) > - < T(z = d, t) >$ between mean temperatures at free surface and bottom as a function of time. The typical evolution

is displayed in figure C.4. A deviation from the pure diffusive state (thick line which is obtained by setting $Ra_{th} = Ma_{th} = 0$) is taken as a signature of free convection onset. Quantitatively a time $t_{on}^{*(nl)}$ (where superscript "*nl*" stands for "nonlinear") can be exhibited that corresponds to the moment where the norm of the dimensionless velocity becomes greater than a threshold. This threshold which characterizes the deviation from pure diffusive state is here defined such that the dimensional velocity becomes greater than the heat diffusion velocity $\kappa/d$. In dimensionless units, it corresponds to $\| \boldsymbol{v}^* \|_2 > 1$ (Touazi et al. [45]). Since it depends on the initial perturbation amplitude and on the threshold, there is some blurredness in the evaluation of time $t_{on}^{*(nl)}$. On the contrary, the saturated nonlinear regime reached after $t_{on}^{*(nl)}$ is independent on the initial state (see figure C.4). This subsequent regime is called quasi-steady in the following since the temperature difference varies much less during this period than during the period close to time of convection onset. Note that, at time $t_{on}^{*(nl)}$, one may obtain the average cell-to-cell distance providing a wavenumber $k_{on}^{*(nl)}$.
The same qualitative behavior is observed in the solutal problem for $< \varphi_s(z = 0, t) > - < \varphi_s(z = d(t), t) >$ (see figure C.5 for the equivalent experimental configuration). The method is then similar, the threshold corresponding to $\| \boldsymbol{v}^+ \|_2 > 1$.

### *4.2. Time and wavenumber corresponding to Convection Onset: Linear Approaches*

Other methods which are used to determine convection onset are quite different being based on linear arguments. They are here presented only for the thermal problem with infinite aspect ratio. The linear theory accounts for the dynamics of infinitesimal perturbations $\boldsymbol{v}_p^*(x^*, z^*, t^*)$, $\theta_p(x^*, z^*, t^*)$, $p_p^*(x^*, z^*, t^*)$ superposed near the purely diffusive basic state $\theta_{BS}(z^*, t^*)$ (which is simulated setting $Ra_{th} = Ma_{th} = 0$). They are assumed of the form

$$(\boldsymbol{v}_p^*, \theta_p, p_p^*) = (\hat{v}_x(z^*, t^*), \hat{v}_z(z^*, t^*), \hat{\theta}(z^*, t^*), \hat{p}(z^*, t^*)) \exp(ik^* x^*) \qquad (30)$$

where $k^*$ denotes the nondimensional wavenumber along the $x^*$ direction. The complex amplitude of the perturbations are governed by the linear system

$$ik^*\hat{v}_x + \frac{\partial \hat{v}_z}{\partial z^*} = 0, \tag{31}$$

$$\frac{1}{Pr}\frac{\partial}{\partial t^*}\hat{v}_x + ik^*\hat{p} - \left[\frac{\partial^2}{\partial z^{*2}} - k^{*2}\right]\hat{v}_x = 0, \tag{32}$$

$$\frac{1}{Pr}\frac{\partial}{\partial t^*}\hat{v}_z + \frac{\partial \hat{p}}{\partial z^*} - \left[\frac{\partial^2}{\partial z^{*2}} - k^{*2}\right]\hat{v}_z - Ra_{th}\,\hat{\theta} = 0, \tag{33}$$

$$\frac{\partial}{\partial t^*}\hat{\theta} + \hat{v}_z\frac{\partial \theta_{BS}}{\partial z^*} - \left[\frac{\partial^2}{\partial z^{*2}} - k^{*2}\right]\hat{\theta} = 0, \tag{34}$$

$$\hat{v}_z = 0, \quad \partial_{z^*}\hat{v}_x + Ma_{th}\,ik^*\hat{\theta} = 0, \qquad \partial_{z^*}\hat{\theta} + Bi\,\hat{\theta} = 0, \quad \text{at } z^* = 1, \tag{35}$$

$$\hat{v}_x = \hat{v}_z = 0, \quad \frac{\partial \hat{\theta}}{\partial z^*} = 0 \quad \text{at } z^* = 0. \tag{36}$$

In this linear framework, various alternatives are possible to evaluate the time of convection onset. First, one may use a frozen-time approximation which considers at each time $t^*$ the unsteady temperature basic profile $\theta_{BS}(z^*, t^*)$ and applies the classical normal mode stability method to this frozen state $\theta_{BS}(z^*, t^*)$. The first time for which the stability spectrum of all wavenumbers contains an eigenvalue with a zero real part, is defined as the onset time $t_{on}^{*(fr)}$. This naturally leads to a critical wavenumber $k_{on}^{*(fr)}$ as well.

Another linear approach explicitly takes into account the unsteady character of basic profile $\theta_{BS}(z^*, t^*)$. It is based on the non-normal method (for details see Doumenc et al. [12]). For the non-autonomous system (31)-(36), the standard notion of growth rate based on eigenvalues is no more valid. One should resort to amplification gains as a function of time to characterize the flow stability. Given an initial disturbance profile, a time $t^*$, and a wavenumber $k^*$, one defines two different norms $E_V$ and $E_T$ for the perturbation amplitudes. The first norm is based on the kinetic energy of perturbations

$$E_V(t^*, k^*) \equiv \int (\hat{v}_x(z^*, t^*, k^*)\hat{v}_x^{\#}(z^*, t^*, k^*) + \hat{v}_z(z^*, t^*, k^*)\hat{v}_z^{\#}(z^*, t^*, k^*))\mathrm{d}z^* \tag{37}$$

where superscript # denotes complex conjugation. The integration is performed over the entire layer height and perturbations are obtained after integrating the

above linear non-autonomous system (31)-(36) over the time period $[0, t^*]$. The second norm is based not on the velocity field but on the temperature field:

$$E_T(t^*, k^*) \equiv \int \hat{\theta}(z^*, t^*, k^*)\hat{\theta}^{\#}(z^*, t^*, k^*)\mathrm{d}z^* \tag{38}$$

The amplification gain at time $t^*$ and for each wavenumber $k^*$ is then evaluated by computing factor $E_V(t^*, k^*)/E_V(0, k^*)$ or $E_T(t^*, k^*)/E_T(0, k^*)$. Given a norm, the non-modal analysis solves an optimization problem based on an iteration procedure and the introduction of an adjoint problem (Farrell and Ioannou [14], Andersson et al. [1], Luchini [22], Schmid and Henningson [40]) which allows: (a) to determine, for given wavenumber $k^*$ and time $t^*$, the maximum energy amplification $\hat{G}(t^*, k^*) \equiv Max[E(t^*, k^*)/E(0, k^*)]$ over all possible initial perturbations profiles; and (b) to exhibit the optimal perturbation mode defined by its initial $z^*-$profile, which actually reaches this upper bound (Schmid and Henningson [40]).

Using the value $\hat{G}(t^*; k^*)$, it is feasible to extend to unsteady flows the usual concepts of classical stability analysis. For instance, $\hat{G}(t^*; k^*)$ can be maximized over wavenumber $k^*$ providing a maximum amplification $G_{max}(t^*)$. This value is effectively reached for a specific wavenumber $k^*_{max}(t^*)$ and for a specific initial perturbation structure in $z^*$. These latter two quantities play the role of the most amplified wavenumber and of the most amplified mode for the standard analysis but at a given time $t^*$. Let us now consider a threshold $G_{thres}$. When the system is capable to reach such a value $G_{thres}$, the basic flow is considered as unstable. The first time when $G_{max}(t^*) = G_{thres}$ defines a new time $t^{*(nn)}_{on}$ of convection onset (where superscript "nn" stands for non-normal) and an associated wavenumber $k^{*(nn)}_{on} = k^*_{max}(t^{*(nn)}_{on})$.

*4.3. Comparisons between approaches*

By varying the threshold value $G_{thres}$, the non-normal analysis provides an interval of times $t^{*(nn)}_{on}$ shown in figure C.6 in the pure Marangoni case. Between $G_{thres} = 1$ and 100, $t^{*(nn)}_{on}$ varies by one decade, and there is only a slight variation between $G_{thres} = 100$ and $10^4$. It is a nice feature of this method to define

a bandwidth of uncertainty, which is inherent here to the transient character of the problem. Results obtained from the nonlinear approach, in which the uncertainty arises because of the unknown amplitudes of initial perturbations are similar to those obtained by the non-normal approach for $G_{thres} \gtrsim 100$. Finally the frozen-time approach provides a value $t_{on}^{*(fr)}$ which is always a lower bound for $t_{on}^{*(nn)}$ or $t_{on}^{*(nl)}$.

Figure C.7 indicates that the same comments apply for the critical wavenumber $k_{on}^{*(nl)}$, $k_{on}^{*(fr)}$, $k_{on}^{*(nn)}$, thus demonstrating that nonlinear and non-normal approaches for $G_{thres} \gtrsim 100$, though of a different nature, give equivalent results.

Based on this remark, in most of the cases considered in this work, we will mainly use the nonlinear approach to determine the conditions of convection onset. Moreover direct numerical simulations also give a more complete description by providing velocity fields in the nonlinear regime and time evolution of the wavelengths.

### *4.4. Critical Control Parameters*

For some sets of control parameters $(Ma_{th}, Ra_{th}, Bi, Pr)$, the critical times $t_{on}^{*(nn)}$, $t_{on}^{*(fr)}$ or $t_{on}^{*(nl)}$ cannot be defined. For instance, this happens in the non-normal mode approach when $G_{max}(t^*)$ always remains below $G_{thres}$. In that case, convection is predicted not to occur and the system to be stable through the instability mechanism considered. Critical Rayleigh or Marangoni numbers can be then defined as the smallest Rayleigh or Marangoni numbers for which times of convection onset appear. In the control parameters space, a marginal stability curve such as $Ra_{th}^c(Bi, Ma_{th}, Pr)$ can also be computed, each point of the curve being associated to critical optimal time $t_c^* = t_{on}^*(Ra_{th}^c, Ma_{th}, Bi, Pr)$ and a critical wavenumber $k_c^* = k_{on}^*(Ra_{th}^c, Ma_{th}, Bi, Pr)$. The results of marginal stability curve has been extensively analyzed in previous studies. See Doumenc et al. [12], Touazi et al. [45] for the critical conditions of the thermal problem, and Trouette et al. [48] for the solutal problem. Here it is introduced because of the comparison with experiments performed in section 5.1.

## 5. Comparisons of numerical predictions with results of PIB/toluene experiments.

### *5.1. Comparisons of critical control parameters*

Experimental data and previous numerical results for thermal and solutal models which provided stability thresholds are gathered in figure C.8. The diagram is drawn in the initial thickness/viscosity plane for the PIB/toluene solution (the initial viscosity is related to the initial polymer volume fraction through equation 17).

The theoretical thresholds separate the diagram in three regions (a) a stable region for both solutal and thermal mechanisms; (b) a region where solutal Bénard-Marangoni mechanism generates an instability; (c) a region where both solutal and thermal mechanisms generate an instability.

The frontier delimiting the observation of convection in PIB/toluene experiments is in agreement with the region of transition from stable to unstable configurations for the thermal Rayleigh-Bénard-Marangoni problem (two continuous lines in figure C.8). Indeed no convection was observed for configurations in which solutal convection is expected (empty squares in figure C.8). This seems paradoxical since, based only on marginal curves, the solutal Bénard-Marangoni mechanism appears to be the most unstable (an exception would be the lowest viscosities corresponding to solutions very close to pure solvent, where solutal convection is not defined). In addition, the predominance of solutal with respect to thermal instability given by theoretical model agrees with previous works (de Gennes [10], Machrafi et al. [23]). This paradox is explained in section 5.3.

In the subsections below, we focus on configurations above the thermal and solutal stability thresholds.

### *5.2. Comparisons of $t^*_{on}$ when thermal and solutal problems are both unstable*

From figure C.8, one can deduce that test cases 1 and 2 in table 1 (indicated by green circles in figure C.8) are clearly unstable for both thermal and solutal problems. The times of convection onset obtained by numerical simulations or

| | Case 1 | Case 2 |
|---|---|---|
| Thermal model | [0.6 - 3] | [14 - 60] |
| Solutal model | [0.8 - 2] | [2 - 7] |
| Experiments | $\lesssim 1$ | $\lesssim 10$ |

Table 2: Time (in seconds) corresponding to the onset of convection: comparison of 2D numerical simulations and experiments for cases 1 and 2

experimental visualizations are compared in table 2. The time intervals given for models correspond to different initial perturbation amplitudes. In experiments, the time visualization at which the pattern becomes clearly visible is estimated similar by iriodin particles or infrared camera. It corresponds to an upper bound of the time of onset.

Despite the large Lewis number ($Le \equiv \kappa/D \sim 10^3$), models show that solutal convection appears at least concomitantly and generally before the thermal one. This is related to the fact that the two cases are far from the solutal Marangoni stability frontier but close to the thermal one (figure C.8). Time of onset for the solutal model is consistent with the experimental estimation for both test cases. The thermal model is also consistent with test case 1 experiment, and the discrepancy with test case 2 is very weak. This analysis is hence not sufficient to determine in a clear cut manner the nature of the observed flow.

### *5.3. Comparisons of wavelengths and velocities when thermal and solutal problems are both unstable*

The wavelengths obtained by numerical simulation or experimental visualization are compared in figure C.9. For both test cases, the observed wavelengths are in very good agreement with the thermal model results while the solutal wavelengths are significantly lower. This is true near the onset but remains so in the later saturated regime.

The preponderance of the thermal mechanism for the two configurations is confirmed by the quantification of velocities (see figure C.10). Velocities induced by thermal effects predominate over the one of solutal origin: thermal velocities are an order of magnitude larger than solutal ones for test case 1, half a decade for test case 2. When the thermal convection is not active, velocities induced by

solutal gradients exist but are too small to be detected by visualization used in the mentioned experiments (see section 6.2 for a more general argument). This explains the paradox mentioned in subsection 5.1. As a conclusion, the analysis of these two test cases clearly highlights the need for a complete characterization of convective regimes to determine the dominant mechanism. Beyond threshold estimation, the saturating amplitude of the instability is also an important parameter.

## 6. Quasi-steady regime in the Bénard Marangoni convection.

Previously, we have seen that estimating the velocity field in the quasi-steady regime may be a way to determine which is the instability mechanism that predominates when both mechanisms are simultaneously unstable. Here we focus on the quasi-steady regime where it is possible to establish scaling laws for velocity field and thus to compare thermal to solutal contributions.

This generalization is performed for the Bénard-Marangoni problem taking into account both thermal and solutal effects but neglecting buoyancy ($Ra_{th} = Ra_{sol} = 0$). This is a relevant assumption for thin films encountered in coating applications.

### *6.1. Scaling laws and comparison with numerical simulations*

Based on some simplifying assumptions, scaling laws are obtained by "solving" equations of thermal and solutal models in terms of order of magnitude. All the equations below and in Appendix B must be hence understood as orders of magnitude only since these scalings do not give prefactors. Note that this approach is similar to the analysis of a transient free convection problem described in Bejan [3], and has already been applied to the thermal Bénard-Marangoni problem in an evaporative liquid (Touazi et al. [45]). In the following, the notation "$x \lesssim y$" (resp. "$x \gtrsim y$") stands for "$x \sim y$ or $x \ll y$" (resp. "$x \sim y$ or $x \gg y$"). The main assumptions are as follows:

H1 Below the free surface, we assume the existence of a hydrodynamic, a thermal as well as a solutal boundary layer of respective thicknesses $\delta_H$, $\delta_T$ and $\delta_S$.

H2 Time derivative terms are neglected (quasi-steady regime).
H3 Temperature (resp. solvent concentration) variations across a convective cell in the vertical and horizontal directions are of same order of magnitude. They are denoted by $\Delta\theta$ (resp. $\Delta\phi_s$).
H4 The wavelength of convective structures scales with the layer thickness. Hence the order of magnitude of the dimensionless characteristic length in the horizontal direction is one.
H5 The analysis is restricted to fluids characterized by a Prandtl number $Pr \gtrsim 1$ (resp. Schmid number $Sc \gtrsim 1$).
H6 Even for solutal model, viscosity and layer thickness are assumed constant and equal to their initial values. This is valid since we focus on the beginning of drying.

Scaling analysis of the thermal problem and its validation by comparison with numerical simulations have been presented in a previous paper (see Touazi et al. [45]). Scaling laws of the solutal configuration are derived in Appendix B. Table 3 summarizes the overall results obtained for velocity and temperature or concentration variations as a function of the relevant dimensionless numbers. Different domains are delineated: domain A (no convection) and domains B, C, D, E which correspond to different cases for $\delta_H$, $\delta_T$ and $\delta_S$. The frontiers delimiting such domains are given in table 4. An illustration of the different domains is given in figure C.11 for the solutal problem and $Sc = 2.3 \times 10^5$ (value of $Sc$ corresponding to test case 2).

Solutal scaling laws have been tested *via* numerical simulations by getting, at the beginning of the quasi-steady state, the L2 norm of the free surface velocity. Several configurations have been considered, all in the B domain. They are based on PIB/toluene or PS/toluene systems, assuming variable or constant viscosity and different values of aspect ratio $A$. Figure C.12 shows that in all cases, results of numerical simulations compare very well with the scaling law, over three decades of $Ma_{sol}$. The free surface velocity prefactor deduced by fit is about 0.2.

As a final comment, this analysis assumes *a priori* the existence of convection

patterns and of quasi-steady regime. Frontiers obtained by this analysis must be compatible with this assumption. Region A (no convection) cannot be thus determined using simply this approach and necessitates the use of a stability analysis. This has been done for the thermal problem for $10^{-3} < Bi < 10^{3}$ (Doumenc et al. [12]). For the solutal model, numerical simulations for $Pe_{int} \lesssim 1$ gives $Ma_{sol} \simeq 100$ (see Trouette et al. [48]) which is consistent with the scaling $Ma_{sol} \sim 1$ for the A-B frontier (see figure C.11).

| | Thermal problem | | | | Solutal problem | | |
|---|---|---|---|---|---|---|---|
| domain | $\delta_H$ | $\delta_T$ | $\Delta\theta$ | scaling laws | $\delta_H$ | $\delta_S$ | scaling laws |
| A | no convection | | | | | | |
| B | $\sim 1$ | $\ll 1$ | $\ll 1$ | $\delta_T \sim (Ma_{th}.Bi)^{-1/3}$<br>$\Delta\theta \sim Ma_{th}^{-1/3}.Bi^{2/3}$<br>$v_x^* \sim (Ma_{th}.Bi)^{2/3}$ | $\sim 1$ | $\ll 1/Pe_{int}$ | $\delta_S \sim Ma_{sol}^{-1/3}$<br>$\Delta\phi_s \sim Ma_{sol}^{-1/3}$<br>$v_x^+ \sim Ma_{sol}^{2/3}$ |
| C | $\sim 1$ | $\ll 1$ | $\sim 1$ | $\delta_T \sim Ma_{th}^{-1/2}$<br>$v_x^* \sim Ma_{th}$ | $\sim 1$ | $\sim 1/Pe_{int}$ | $\Delta\phi_s \sim Ma_{sol}^{-1}.Pe_{int}^{2}$<br>$v_x^+ \sim Pe_{int}^{2}$ |
| D | $\ll 1$ | $\ll 1$ | $\sim 1$ | $\delta_T \sim Ma_{th}^{-1/3}.Pr^{-1/6}$<br>$\delta_H \sim Ma_{th}^{-1/3}.Pr^{1/3}$<br>$v_x^* \sim Ma_{th}^{2/3}.Pr^{1/3}$ | $\ll 1$ | $\sim 1/Pe_{int}$ | $\Delta\phi_s \sim Ma_{sol}^{-1}.Sc^{-1/2}.Pe_{int}^{3}$<br>$\delta_H \sim Sc^{1/2}.Pe_{int}^{-1}$<br>$v_x^+ \sim Pe_{int}^{2}$ |
| E | $\ll 1$ | $\ll 1$ | $\ll 1$ | $\delta_T \sim (Ma_{th}.Bi)^{-1/4}.Pr^{-1/8}$<br>$\delta_H \sim (Ma_{th}.Bi)^{-1/4}.Pr^{3/8}$<br>$\Delta\theta \sim Ma_{th}^{-1/4}.Bi^{3/4}.Pr^{-1/8}$<br>$v_x^* \sim (Ma_{th}.Bi)^{1/2}.Pr^{1/4}$ | $\ll 1$ | $\ll 1/Pe_{int}$ | $\delta_S \sim Ma_{sol}^{-1/4}.Sc^{-1/8}$<br>$\delta_H \sim Ma_{sol}^{-1/4}.Sc^{3/8}$<br>$\Delta\phi_s \sim Ma_{sol}^{-1/4}.Sc^{-1/8}$<br>$v_x^+ \sim Ma_{sol}^{1/2}.Sc^{1/4}$ |

Table 3: Quasi-steady regime in the BM configuration - Scaling laws.

### *6.2. Comparison of thermal and solutal velocities*

From comparison of scaling analysis with numerical simulations, the domain explored in typical drying experiments like test case 1 is shown to correspond

| domain | domain | boundary equation thermal problem | boundary equation solutal problem |
|---|---|---|---|
| A | B | $Bi \times Ma_{th} \sim 1$ | $Ma_{sol} \sim 1$ |
| A | C | $Bi \sim Ma_{th}$ | unknown |
| B | C | $Bi^2 \times Ma_{th}^{-1} \sim 1$ | $Ma_{sol} \sim Pe_{int}^{3}$ |
| B | E | $Bi^{2/3} \times Ma_{th}^{2/3} \sim Pr$ | $Ma_{sol} \sim Sc^{3/2}$ |
| C | D | $Ma_{th} \sim Pr$ | $Pe_{int} \sim Sc^{1/2}$ |
| D | E | $Bi^6 \times Ma_{th}^{-2} \sim Pr$ | $Ma_{sol} \sim Pe_{int}^{4}.Sc^{-1/2}$ |

Table 4: Quasi-steady regime in the BM configuration - boundaries between the different domains.

to B domains. This is true in thermal and solutal problems. Let us use the scalings of table 3 to compare thermal and solutal velocities.

$$\frac{v_x^*}{v_x^+} \sim \left[\frac{Ma_{th}.Bi}{Ma_{sol}}\right]^{2/3}, \tag{39}$$

or in dimensional quantities:

$$\frac{v_{th}}{v_{sol}} \sim Le^{-1/3} \quad \left[\frac{\gamma_{th} Lc^{-1}}{\gamma_{sol}}\right]^{2/3} \quad \varphi_{pi}^{-2/3} \quad \left[\frac{Q_m}{\rho v_{ev}}\right]^{2/3} \tag{40}$$

with $Le \equiv \kappa/D$ the Lewis number, $c$ the heat capacity ($c = \lambda/(\rho\kappa)$) and $Q_m$ the evaporation flux at the beginning of the drying. The two first terms depend on the system properties only, the two last ones on experimental conditions. The Lewis number compares the solutal diffusion characteristic time to the thermal one. It is of order of $10^3$ for both PIB/toluene and PS/toluene solutions. The second dimensionless number (between square brackets) compares the two driving mechanisms ($\simeq 5.2$ for PIB/toluene, 3.5 for PS/toluene). Notice that the difference between the evaporation flux at the beginning of the drying $Q_m$ and during the regime at constant evaporation flux ($\rho v_{ev}$) is due to evaporation cooling effect. Nevertheless, they are very close (the ratio is about 1.3 for the test case 2, cf. figure C.1), so that the last term of Eq. 40 will be equal to one as an order of magnitude.

Remarkably enough, the ratio of the thermal and solutal velocities does not depend on the sample thickness (see Eq. 40). For a quantitative comparison, note that the prefactors obtained through numerical simulations are close to 0.2 for thermal (see Touazi et al. [45]) and solutal problem (figure C.12). Hence, for both solutions (PIB or PS in toluene), the ratio of the thermal and solutal velocities thus reads

$$\frac{v_{th}}{v_{sol}} \simeq 0.3\ \varphi_{pi}^{-2/3} \tag{41}$$

The above result has been derived for pure Marangoni configurations, i.e. neglecting buoyancy, and assuming that both thermal and solutal problems are unstable. In such a configuration, it leads to the following conclusion: when the thermal and solutal mechanisms are both involved, comparison of stability

thresholds or critical times is not sufficient. It is also necessary to consider the velocities induced by the two phenomena. For dilute solutions (e.g. $\varphi_{pi} = 0.006$ as in experimental test case 1), the thermal velocity is one order of magnitude higher than the solutal one, which is consistent with the result presented in figure C.10. The two velocities would reach the same order of magnitude for $\varphi_{pi} \simeq 0.2$. Higher polymer volume fraction would induce very high viscosity (see figure C.3), so we can conclude that, for the two polymer solutions under investigation, if thermal convection is present, it could hardly be dominated by solutal convection.

*6.3. Comparison with PS/toluene experiments*

The set of experiments performed by Bassou and Rharbi [2] concerns thin PS/toluene films with initial thickness $d_i = 1.4$ mm. Experimental configurations and corresponding dimensionless numbers are detailed in table 1 (cases 3 to 5). Velocity measurements have been performed using the particle tracking method, with an optical microscope connected to a CCD camera. This method allows the measurement of small velocities (a few $\mu$m.s$^{-1}$, cf. Bassou and Rharbi [2] for experimental details). Using the critical Rayleigh and Marangoni numbers from Doumenc et al. [12] for the thermal problem, and from Trouette et al. [48] for the solutal problem, it is possible to show that these configurations are all stable for the thermal and solutal Rayleigh-Bénard problem as well as the thermal Bénard-Marangoni problem, and unstable for the solutal Bénard-Marangoni problem. This confirms that the flow observed in experiments can only be driven by solutal surface tension gradients, as stated by Bassou and Rharbi in their article. The mechanism of cells formation in these experiments being clearly known, the measured velocities can be used for comparison with the numerical simulations of the solutal Bénard-Marangoni problem. Velocities measured close to the free surface at the beginning of the drying in the nonlinear quasi-steady regime are plotted in figure C.12 (the error bars give the minimum and maximum values measured during the first 1000 s). There are not enough experimental data to conclude on the validity of the scaling presented in section

3, but comparison with numerical simulations reveals that the model overestimates the experimental results by a factor 3. Even if this discrepancy does not put into questions the conclusions of the paper based on comparison of order of magnitudes, it is interesting to understand its origin. This difference seems too high to be explained by experimental uncertainties (velocity measurement) or by uncertainties over system properties (viscosity, diffusion coefficient,...) or else by the choice of velocity L2 norm to express surface velocity from numerical simulations. The reason of such a discrepancy should hence be attributed to some model assumptions. Soret effect is neglected, but this assumption seems correct: using the scaling laws from table 3 (see Appendix C), it is shown that Soret effect generates a polymer flux which is about two orders of magnitude lower than the flux driven by the concentration gradient due to evaporation. Turning to the modelling of the free surface, solution surface tension is expressed as a function of bulk concentration near the interface (see Eq. 16). Surface tension actually depends on the surface concentration. In order to get a univoque relationship between the bulk concentration near interface and the surface concentration itself, local thermodynamic equilibrium between the bulk and the interface must be satisfied. Otherwise (out of equilibrium surface), one should consider the dynamic of the solvent transport at the free surface, as it has already been done with soluble surfactants (see for example Yiantsios and Higgins [56], Shklyaev, S. and Nepomnyashchy, A.A. [43]). This would necessitate a more elaborate model, but also experiments performed with well characterized polymer solutions for its validation.

## 7. Conclusion

In this study, we present a detailed analysis of free convection occuring during the drying of plane layers of polymer solutions. Four mechanisms, based on buoyancy or Marangoni effect, of thermal or solutal origin, are taken into account. We show that when a configuration is unstable for several mechanisms, the comparison of stability thresholds may be insufficient to predict which mechanism dominates: a nonlinear approach is then needed. This theoretical and

numerical work combined with previous studies (Doumenc et al. [12], Touazi et al. [45], Trouette et al. [48]) provides all the required tools to analyze thoroughly the problem.

First, different methodologies are proposed in a transient problem to predict the critical time for convection onset. Nonlinear and non-normal methods give similar results, within the uncertainty inherent to any transient problem. We then focus on two configurations unstable for both the thermal and the solutal problem. The comparison of critical times, which is the information that a linear approach could give, does not allow to discriminate. Nonlinear 2D simulations show that temperature gradients produce higher velocities than concentration gradients. We have thus exhibited configurations where thermal mechanism is dominant, while a simple comparison of stability thresholds would have lead to the reverse conclusion. When comparing to experimental results, a very good agreement between simulated thermal wavelengths and experimental ones are obtained.

Finally, using scaling arguments, we derive a general description of the nonlinear quasi-steady regime for the Bénard-Marangoni configuration. Correlations have been obtained for the thermal and solutal problem and validated by numerical simulations. One important result is the estimation of the ratio of the thermal velocity to the solutal velocity (Eq.40), which gives a simple relation to easily estimate the relative importance of the two mechanisms. It would be useful to derive the same type of relation for other systems than polymer solutions, for instance water/ethanol, where both components are volatile. In the present work thermal and solutal mechanisms have been decoupled, in order to highlight their respective roles for experiments where both mechanisms lead to unstable configuration. Next step should concern the development of a complete thermal-solutal model to put forward coupled effects. This would be necessary to analyse longer times, when the increase of viscosity due to the decrease of solvent concentration induces a coupling between the thermal and solutal problems (this can result in the formation of a crust, observed in experiments by Toussaint et al. [46]). The coupling between the two problems

should also be needed to perform a more detailed analysis, like for instance 3D pattern evolution, especially when the thermal and solutal mechanisms lead to comparable velocities. Another problem requiring coupled models concerns the case of thermal and solutal mechanisms acting in opposite way, one stabilizing the system.

Acknowledgments: TB and MR acknowledge financial support from the Deutsche Forschungsgemeinschaft in the framework of the priority program "Transport Processes at Fluidic Interfaces" (grant Bo 1668/6). FD and BG acknowledge financial support from the European Union via the FP7 Marie Curie scheme (grant PITN-GA-2008- 214919 (MULTIFLOW)). FD, BT, EC, CD and BG acknowledge financial support from the Fédération TMC (Ministère de l'Enseignement supérieur et de la Recherche, France).

## Appendix A. Physical properties of PIB/toluene and PS/toluene solutions

### Viscosity

To take into account the variation of the solution viscosity with solvent concentration, we use the empirical law interpolated from measurements (data from Gorand et al. [17], Mark [25] for PIB/toluene, Bassou and Rharbi [2] for PS/toluene):

$$\log_{10}(\mu) = a_0 \; + \; a_1\, Y \; + \; a_2\, Y^2 \; + \; a_3\, Y^3 \; + \; a_4\, Y^4 \qquad \text{(A.1)}$$

with $Y = \log_{10}(\varphi_p)$, $(a_0, a_1, a_2, a_3, a_4) = (8.235, 14.02, 6.575, 1.392, 0.1114)$ for PIB/toluene and $(3.361, 6.7733, 2.4433, 0.30432, 0)$ for PS/toluene (see figure C.3).

### Mutual diffusion coefficient

To the best of our knowledge, there is no available data in the literature for the mutual diffusion coefficient of PIB/toluene solutions at room temperature, for the concentration range covered by our experiments. Nevertheless, a rough estimate $D \simeq 10^{-10}$ m$^2$s$^{-1}$ can be obtained by extrapolating measurements performed in the concentrated regime by Doumenc et al. [13].

On the contrary, the mutual diffusion in PS/toluene system has been widely characterized. Values in table A.5 have been obtained by averaging data from Roots and Nyström [36], Brown et al. [6], Zhang et al. [59] at temperature 25°C and Rauch and Kohler [32] at temperature 22°C.

| $\varphi_p$ | 0.10 | 0.15 | 0.20 |
|---|---|---|---|
| $D \times 10^{10}/m^2.s^{-1}$ | $1.25 \pm 0.15$ | $1.60 \pm 0.15$ | $1.85 \pm 0.25$ |
| $S_T\ /K^{-1}$ | 0.074 | 0.057 | 0.047 |

Table A.5: Mutual diffusion coefficient $D$ and polymer Soret coefficient $S_T$ of PS/toluene solution at room temperature as a function of polymer volume fraction (from Roots and Nyström [36], Brown et al. [6], Zhang et al. [59], Rauch and Kohler [32] for $D$, the two last references also provide $S_T$). The uncertainty range of $D$ represents the scattering over the different sources. The differences between $S_T$ values from Zhang et al. [59] and Rauch and Kohler [32] are lower than the experimental uncertainty, which is around $10^{-3}$.

### Other physical properties

Some properties of PIB/toluene and PS/toluene solutions are assumed to be equal to those of pure toluene (from Riddick et al. [35], Monteil and Postel [28])

$$\kappa = 0.97 \times 10^{-7}\ \ m^2.s^{-1},\ \ \lambda = 0.142\ \ W.m^{-1}.K^{-1},\ \ L = 3.96 \times 10^5 J.kg^{-1},$$

$$\rho_0(T = 20^0C) = 870\ \ kg.m^{-3},\ \ \alpha_{th} = 1.07 \times 10^{-3}\ \ K^{-1},$$

$$\sigma_0(T = 20^0C) = 28.5 \times 10^{-3}\ \ N.m^{-1},\ \ \gamma_{th} = 1.19 \times 10^{-4}\ \ N.m^{-1}.K^{-1},$$

Specific properties of the PIB/toluene solution are the following ones (cf. [46, 25] for details):
PIB molar mass: $M_w = 500\ kg.mol^{-1}$, $\rho_{PIB} \simeq 920\ \ kg.m^{-3}$, $\alpha_{sol} = 5.82 \times 10^{-2}$, $\gamma_{sol} = 5.4 \times 10^{-3}\ \ N.m^{-1}$.
Specific properties of the PS/toluene solution are the following ones (cf. [2, 25] for details):
PS molar mass: $M_w = 150\ kg\ mol^{-1}$, $\rho_{PS} \simeq 1050\ \ kg.m^{-3}$, $\alpha_{sol} = 0.21$, $\gamma_{sol} = 8.0 \times 10^{-3}\ \ N.m^{-1}$. Soret coefficient is reported in table A.5.

## Appendix B. Quasi-steady regime in the Bénard-Marangoni solutal convection: scaling laws

In this appendix, scaling laws for the Bénard-Marangoni solutal convection are derived in the quasi-steady regime. Since we consider the beginning of the quasi-steady regime, we assume $d \sim d_i$, $\mu \sim \mu_i$ and $\varphi_s \sim \varphi_{si}$ in the bulk (i.e. below the solutal boundary layer). From these assumptions and after the removal of time partial derivatives (quasi-steady regime), governing equations (22), (23) and (24) read (for clarity sake, supercripts + are omitted on dimensionless variables):

$$\partial_x v_x + \partial_z v_z = 0, \tag{B.1}$$

$$\frac{1}{Sc}(v_x \partial_x v_x + v_z \partial_z v_x) = -\partial_x p + \partial_x^2 v_x + \partial_z^2 v_x, \tag{B.2}$$

$$\frac{1}{Sc}(v_x \partial_x v_z + v_z \partial_z v_z) = -\partial_z p + \partial_x^2 v_z + \partial_z^2 v_z, \tag{B.3}$$

$$v_x \partial_x \phi_s + v_z \partial_z \phi_s = \partial_x^2 \phi_s + \partial_z^2 \phi_s. \tag{B.4}$$

If one eliminates the pressure gradient term from equations (B.2) (B.3), an equation for vorticity $\omega$ is derived

$$v_x \partial_x \omega + v_z \partial_z \omega = Sc(\partial_x^2 + \partial_z^2)\omega \;\text{ with }\; \omega \equiv \partial_z v_x - \partial_x v_z \tag{B.5}$$

which expresses a balance between inertia (left-hand side) and friction (right-hand side) in the hydrodynamic boundary layer. Finally boundary conditions become at the bottom

$$v_x = v_z = 0, \qquad \partial_z \phi_s = 0 \qquad \text{at } z = 0 \tag{B.6}$$

and at the upper surface

$$\partial_z \phi_s + 1 - Pe_{int} \phi_s = 0 \tag{B.7}$$

$$\partial_z v_x + Ma_{sol}\, \partial_x \phi_s = 0. \tag{B.8}$$

$$v_z = 0. \tag{B.9}$$

Scaling laws are obtained by solving equations B.1 to B.9 in terms of order of magnitude. From now on, all quantities are thus intended to be orders of

magnitude. The continuity equation (B.1) coupled to hypotheses H1 and H4 (see section 6) imposes

$$v_z \sim \delta_H v_x \tag{B.10}$$

From hypoteses H1 and H4 and equation (B.5) and assuming $\delta_H \ll 1$ one easily gets

$$v_x \sim \frac{Sc}{\delta_H^2} \tag{B.11}$$

For consistency, this equation is only valid when $\sqrt{S_c/v_x} \ll 1$. When $\sqrt{S_c/v_x} \gtrsim 1$, the hydrodynamic boundary layer thickness saturates at $\delta_H \sim 1$, and inertia is no more involved in the problem.

From equation (B.8), a relation between $\Delta\phi_s \equiv \phi_s(x, z=0) - \phi_s(x, z=1)$ the variation of solvent volume fraction and velocity can be found:

$$v_x \sim \delta_H \; Ma_{sol} \; \Delta\phi_s. \tag{B.12}$$

The transport equation (B.4) expresses the balance between the solvent supplied by convection along the $x$-axis, the solvent supplied by convection along the z-axis, and the diffusion in the liquid. These three terms are respectively of order

$$v_x \Delta\phi_s \; ; \; \hat{v}_z \frac{\Delta\phi_s}{\delta_S} \; ; \; \frac{\Delta\phi_s}{\delta_S^2} \tag{B.13}$$

where $\hat{v}_z$ denotes the magnitude of vertical velocity within the solutal boundary layer. This quantity can be different from $v_z$ the magnitude of vertical velocity within the hydrodynamic boundary layer. By definition $\delta_H \lesssim 1$ and $\delta_S \lesssim 1$. Three cases can then be considered

$$\begin{aligned}
\text{Case 1} &: \quad \delta_\text{H} \ll 1 \qquad \text{and} \qquad \delta_S \lesssim \delta_H \\
\text{Case 1}' &: \quad \delta_\text{H} \ll 1 \qquad \text{and} \qquad \delta_H \lesssim \delta_S \\
\text{Case 2} &: \quad \delta_\text{H} \sim 1 \qquad \text{and} \qquad \delta_S \lesssim \delta_H
\end{aligned}$$

Case 1 implies $\delta_S \lesssim \delta_H$ and thus $\hat{v}_z \sim \frac{\delta_S}{\delta_H} v_z$. The balance between the different terms of (B.13) plus equation (B.10) leads to

$$v_x \sim \delta_S^{-2} \tag{B.14}$$

Case 1' implies $\hat{v}_z \sim v_z$. The balance between the different terms of (B.13) plus equation (B.10) leads to the same equation (B.14).

Case 2 implies $\hat{v}_z \sim \delta_S v_z$. The balance between the different terms of (B.13) plus equation (B.10) leads again to equation (B.14).

When equation (B.14) is compared with equation (B.11) (valid only when $\delta_H \ll 1$), this imposes

$$\delta_S/\delta_H \sim S_c^{-1/2} \quad \text{when} \quad \delta_H \ll 1 \tag{B.15}$$

Since we assume that $Sc \gtrsim 1$, this means that $\delta_S \lesssim \delta_H$ (for $\delta_H \sim 1$, this is obviously true). Note as well that this implies that case 1' is not possible.

Due to the fact that $\phi_s \leq 0$ and $\partial_z \phi_s \leq 0$, the boundary condition (B.7) expresses the balance between only two terms:

$$\frac{\Delta\phi_s}{\delta_S} \sim (1 - Pe_{int}\phi_s) \tag{B.16}$$

Assuming $\phi_s \sim 0$ in the bulk (quasi-steady assumption), we get $\Delta\phi_s \sim -\phi_s$ and the boundary condition (B.7) reads

$$\Delta\phi_s \sim (\delta_S + Pe_{int}\delta_S\Delta\phi_s). \tag{B.17}$$

This equation cannot be verified if $Pe_{int}\delta_S \gg 1$, so only two cases are possible

$$\text{Case } \alpha \ : \qquad \delta_S Pe_{int} \ll 1 \quad \text{then} \quad \Delta\phi_{\mathrm{s}} \sim \delta_{\mathrm{S}} \tag{B.18}$$

$$\text{Case } \beta \ : \qquad \delta_S Pe_{int} \sim 1 \tag{B.19}$$

We must now consider the four combinations of cases 1 or 2 and cases $\alpha$ or $\beta$ taking into account that $\delta_S \lesssim \delta_H$ is always valid. In the following, we only derive explicitly the single case (1 and $\alpha$). Let us assume that cases 1 and $\alpha$ are valid. This means

$$\delta_H \ll 1 \quad \text{and} \quad \delta_{\mathrm{S}}\mathrm{Pe}_{\mathrm{int}} \ll 1 \tag{B.20}$$

Using equations B.11, B.12, B.14 and B.18, it is possible to get expressions for $v_x$, $\delta_S$, $\delta_H$ and $\Delta\phi_s$

$$v_x \sim S_c^{1/4} Ma_{sol}^{1/2} \tag{B.21}$$

$$\delta_H \sim S_c^{3/8} Ma_{sol}^{-1/4} \tag{B.22}$$

$$\delta_S \sim S_c^{-1/8} Ma_{sol}^{-1/4} \tag{B.23}$$

$$\Delta\phi_s \sim S_c^{-1/8} Ma_{sol}^{-1/4}. \tag{B.24}$$

These relations should be compatible with the assumptions which imposes

$$\delta_H \ll 1 \quad \Rightarrow \quad S_c^{3/2} \ll Ma_{sol} \tag{B.25}$$

$$\delta_S Pe_{int} \ll 1 \quad \Rightarrow \quad Pe_{int}^4 S_c^{-1/2} \ll Ma_{sol} \tag{B.26}$$

For the other cases, the method is similar. The synthesis of all the cases are presented in tables 3 and 4. The different domains are displayed in figure C.11.

## Appendix C. Soret effect

Our objective is to show that Soret effect is negligible compared to the diffusion flux driven by the concentration gradient. We consider the configuration of section 6.3 (PS/toluene solution of initial thickness $d_i = 1.4$ mm, test cases 3 to 5), where the solutal Bénard-Marangoni problem is the only one to be unstable.

The polymer diffusive flux $\boldsymbol{j}$ is the sum of the flux $\boldsymbol{j}_f = -D\rho\boldsymbol{\nabla}\omega_p$ driven by the concentration gradient (Fick's law) and the flux $\boldsymbol{j}_s = -D\rho S_T\omega_p\omega_s\boldsymbol{\nabla}T$ driven by the temperature gradient (Soret effect). $S_T$ is the Soret coefficient, $\omega_p$ and $\omega_s$ are the mass fractions of polymer and solvent, respectively. With the assumption of constant density we get:

$$\boldsymbol{j} = \boldsymbol{j}_f + \boldsymbol{j}_s = -D\rho\boldsymbol{\nabla}\varphi_p - D\rho S_T\varphi_p\varphi_s\boldsymbol{\nabla}T \tag{C.1}$$

Soret effect is negligible if the condition $\frac{\|\boldsymbol{j}_s\|}{\|\boldsymbol{j}_f\|} \ll 1$ is satisfied. The order of magnitude of $\|\boldsymbol{j}_f\|$ is readily obtained using the scaling laws of B region in table 3:

$$\|\boldsymbol{j}_f\| \sim D\rho\frac{\Delta\varphi}{d_i}\frac{\Delta\phi_s}{\delta_s} \sim D\rho\frac{\Delta\varphi}{d_i} \tag{C.2}$$

A higher bound of $\|\boldsymbol{j}_s\|$ can be derived from the temperature gradient of the diffusive thermal state (indeed, solutal convection can only decrease the temperature gradient by mixing). For the configurations under consideration, $Bi \lesssim 1$ and the dimensionless temperature gradient reads $\frac{\partial \theta}{\partial z^*} \sim Bi$ (see the study of the thermal basic state by Doumenc et al. [12]). We get:

$$\|\boldsymbol{j}_s\| \lesssim D\rho S_T \varphi_p \varphi_s \frac{\Delta T_{st}}{d_i} Bi \tag{C.3}$$

The desired relation follows:

$$\frac{\|\boldsymbol{j}_s\|}{\|\boldsymbol{j}_f\|} \lesssim Le^{-1} \, (S_T L c^{-1}) \, (\frac{Q_m}{\rho v_{ev}}) \, \varphi_{si} \tag{C.4}$$

with $Le \equiv \kappa/D$ the Lewis number, $L$ the latent heat of vaporization and $c$ the heat capacity. From Appendix A we get $Le \sim 10^3$ and $(S_T L c^{-1}) \sim 10$. The two last terms are of order of 1, so the final result is:

$$\frac{\|\boldsymbol{j}_s\|}{\|\boldsymbol{j}_f\|} \lesssim 10^{-2} \ll 1. \tag{C.5}$$

This result clearly supports the assumption of negligible Soret effect.

## References


[1] Andersson, P., Berggren, M., Henningson, D. S., 1999. Optimal disturbances and bypass transition in boundary layers. Phys. Fluids 11, 134–150.

[2] Bassou, N., Rharbi, Y., 2009. Role of Bénard-Marangoni instabilities during solvent evaporation in polymer surface corrugations. Langmuir 25, 624–632.

[3] Bejan, A., 1984. Convection heat transfer. John Wiley and sons.

[4] Berg, J., Boudart, M., A., A., 1966. Natural convection in pools of evaporating liquids. J. Fluid Mech. 24, 721–535.

[5] Bodenschatz, E., Pesch, W., Ahlers, G., 2000. Recent developments in Rayleigh-Bénard convection. Annu. Rev. Fluid Mech. 32, 709–778.

[6] Brown, W., Johnsen, R. M., Konak, C., Dvoranek, L., 1991. Dynamics in concentrated polymer solutions by polarized Rayleigh-Brillouin scattering and dynamic light scattering. J. Chem. Phys. 95 (11), 8568–8577.

[7] Cammenga, H., Schreiber, D., Barnes, G., Hunter, D., 1984. On Marangoni convection during the evaporation of water. J. Colloid Interface Sci. 98 (2), 585 – 586.

[8] Chénier, E., Desceliers, C., Delcarte, C., Trouette, B., Doumenc, F., Guerrier, B., August 8-13 2010. Sensitivity of diffusive-convective transition to the initial conditions in a transient Bénard-Marangoni problem. In: Proc. EPM-Conference. No. CDROM nI846DV. Washington D.C., USA.

[9] Colinet, P., Legros, J. C., Velarde, M. G., 2001. Nonlinear Dynamics of Surface-Tension-Driven Instabilities. Wiley-VCH.

[10] de Gennes, P., 2001. Instabilities during the evaporation of a film: Non-glassy polymer + volatile solvent. Eur. Phys. J. E 6 (5), 421–424.

[11] de Gennes, P., 2002. Solvent evaporation of spin cast films: crust effects. Eur. Phys. J. E 7, 31–34.

[12] Doumenc, F., Boeck, T., Guerrier, B., Rossi, M., 2010. Transient Rayleigh-Bénard-Marangoni convection due to evaporation : a linear non-normal stability analysis. J. Fluid Mech. 648, 521–539.

[13] Doumenc, F., Guerrier, B., Allain, C., 2005. Mutual diffusion coefficient and vapor-liquid equilibrium data for the system pib/toluene. J. Chem. Eng. Data 50, 983–988.

[14] Farrell, B. F., Ioannou, P. J., 1996. Generalized stability theory part I: autonomous operators. J. Atmos. Sci. 53, 2025–2040.

[15] Foster, T., 1965. Onset of convection in a layer of fluid cooled from above. Phys. Fluids 8 (10), 1770–1774.

[16] Foster, T., 1965. Stability of a homogeneous fluid cooled uniformly from above. Phys. Fluids 8 (7), 1249–1257.

[17] Gorand, Y., Doumenc, F., Guerrier, B., Allain, C., 2003. Instabilités de plissement lors du séchage de films polymères plans. Rhéologie 3, 22–29.

[18] Goussis, D., Kelly, R., 1990. On the thermocapillary instabilities in a liquid layer heated from below. Int J. Heat Mass Transfer 33, 2237–2245.

[19] Guerrier, B., Bouchard, C., Allain, C., Bénard, C., 1998. Drying kinetics of polymer films. AIChE J. 44 (4), 791–798.

[20] Huraux, K., Narita, T., Bresson, B., Fretigny, C., Lequeux, F., 2012. Wrinkling of a nanometric glassy skin/crust induced by drying in poly(vinyl alcohol) gels. Soft Matter 8, 8075–8081.

[21] Jun, S. I., Lee, H. S., 2012. The effect of Bénard-Marangoni convection on percolation threshold in amorphous polymer-multiwall carbon nanotube composites. Current Applied Physics 12 (2), 467 – 472.

[22] Luchini, P., 2000. Reynolds-number-independent instability of the boundary layer over a flat surface: optimal perturbations. J. Fluid Mech. 404, 289–309.

[23] Machrafi, H., Rednikov, A., Colinet, P., Dauby, P., 2010. Bénard instabilities in a binary-liquid layer evaporating into an inert gas. J. Colloid Interface Sci. 349 (1), 331 – 353.

[24] Manneville, P., 2006. Rayleigh-Bénard Convection: Thirty Years of Experimental, Theoretical, and Modeling Work. Springer tracts in Modern Physics, pp. 41–65.

[25] Mark, J. E., 1999. Polymer Data Handbook. Oxford University Press.

[26] Merkt, D., Bestehorn, M., 2003. Bénard-Marangoni convection in a strongly evaporating fluid. Physica D 185, 196–208.

[27] Minařík, A., Smolka, P., Lapčík, L., 2011. Preliminary investigation of factors determining self-organised structures preparation in polymer layers. Int. J. Heat Mass Transfer 54 (1718), 4135 – 4142.

[28] Monteil, C., Postel, M., 1955. Techniques de l'ingénieur. Constantes. Vol. K2.

[29] Moussy, C., Lebon, G., Margerit, J., 2004. Influence of evaporation on Bénard-Marangoni instability in a liquid-gas bilayer with a deformable interface. Eur. Phys. J. B 40, 327–335.

[30] Nepomnyashchy, A. A., Simanovskii, I., Legros, J. C., 2006. Interfacial Convection in Multilayer Systems. Springer.

[31] Pearson, J. R. A., 1958. On convection cells induced by surface tension. J. Fluid Mech. 4, 489–500.

[32] Rauch, J., Kohler, W., 2003. Collective and thermal diffusion in dilute, semidilute, and concentrated solutions of polystyrene in toluene. J. Chem. Phys. 119 (22), 11977–11988.

[33] Rayleigh, L., 1916. On convection currents in a horizontal layer of fluid when the higher temperature is on the under side. Phil. Mag. 32, 529–546.

[34] Reichenbach, J., Linde, H., 1981. Linear perturbation analysis of surface-tension-driven convection at a plane interface (Marangoni instability). J. Colloid Interface Sci. 84, 433–443.

[35] Riddick, J., Bunger, W., Sakano, T., 1986. Organic solvents, physical properties and methods of purification. John Wiley and sons.

[36] Roots, J., Nyström, B., 1980. Cooperative diffusion in semidilute polystyrene solutions at good and solvent conditions. Macromolecules 13 (6), 1595–1598.

[37] Sakurai, S., Furukawa, C., Okutsu, A., Miyoshi, A., Nomura, S., 2002. Control of mesh pattern of surface corrugation via rate of solvent evaporation in solution casting of polymer film in the presence of convection. Polymer 43 (11), 3359 – 3364.

[38] Sakurai, S., Tanaka, K., Nomura, S., 1993. Two-dimensional undulation pattern on free surface of polymer film cast from solution. Polymer 34 (5), 1089 – 1092.

[39] Schatz, M., Neitzel, G., 2001. Experiments on thermocapillary instabilities. Annu. Rev. Fluid Mech. 33, 93–127.

[40] Schmid, P. J., Henningson, D. S., 2001. Stability and Transition in Shear Flows. Springer Verlag.

[41] Scriven, L., Sternling, C., 1964. On cellular convection driven by surface-tension gradients: effects of mean surface tension and surface viscosity. J. Fluid Mech. 19, 321–340.

[42] Serpetsi, S., Yiantsios, S., 2012. Stability characteristics of solutocapillary Marangoni motion in evaporating thin films. Phys. Fluids 24, 122104.

[43] Shklyaev, S., Nepomnyashchy, A.A., 2011. Marangoni instability of a heated liquid layer in the presence of a soluble surfactant. Eur. Phys. J. Special Topics 192, 155–161.

[44] Spangenberg, W. G., Rowland, W. R., 1961. Convective circulation in water induced by evaporative cooling. Phys. Fluids 4 (6), 743–750.

[45] Touazi, O., Chénier, E., Doumenc, F., Guerrier, B., 2010. Simulation of transient Rayleigh-Bénard-Marangoni convection induced by evaporation. Int. J. Heat Mass Transfer 53, 656–664.

[46] Toussaint, G., Bodiguel, H., Doumenc, F., Guerrier, B., Allain, C., 2008. Experimental characterization of buoyancy- and surface tension-driven convection during the drying of a polymer solution. Int. J. Heat Mass Transfer 51, 4228–4237.

[47] Trouette, B., Chénier, E., Delcarte, C., Guerrier, B., 2011. Numerical study of convection induced by evaporation in cylindrical geometry. Eur. Phys. J. Special topics 192, 83–93.

[48] Trouette, B., Chénier, E., Doumenc, F., Delcarte, C., Guerrier, B., 2012. Transient Rayleigh-Bénard-Marangoni solutal convection. Phys. Fluids 24, 074108.

[49] Uchiyama, H., Mantani, Y., Kozuka, H., 2012. Spontaneous formation of linearly arranged microcraters on sol-gel-derived silica-poly(vinylpyrrolidone) hybrid films induced by Bénard-Marangoni convection. Langmuir 28 (27), 10177–10182.

[50] Uchiyama, H., Miki, Y., Mantani, Y., Kozuka, H., 2012. Spontaneous formation of micrometer-scaled cell-like patterns on alkoxide-derived silica gels induced by Bénard-Marangoni convections. The Journal of Physical Chemistry C 116 (1), 939–946.

[51] Uguz, K. E., Narayanan, R., 2012. Instability in evaporative binary mixtures. i. the effect of solutal Marangoni convection. Phys. Fluids 24 (9), 094101.

[52] Uguz, K. E., Narayanan, R., 2012. Instability in evaporative binary mixtures. ii. the effect of Rayleigh convection. Phys. Fluids 24 (9), 094102.

[53] Vidal, A., Acrivos, A., 1968. Effect of nonlinear temperature profiles on onset of convection driven by surface tension gradients. Ind. Eng. Chem. Fundam. 7, 53–58.

[54] Weh, L., 1999. Self-organized structures at the surface of thin polymer films. Mater. Sci. Eng., C 89 (0), 463 – 467.

[55] Yiantsios, S. G., Higgins, B. G., 2006. Marangoni flows during drying of colloidal films. Phys. Fluids 18 (8), 082103.

[56] Yiantsios, S. G., Higgins, B. G., 2010. A mechanism of Marangoni instability in evaporating thin liquid films due to soluble surfactant. Phys. Fluids 22 (2), 022102.

[57] Zhang, J., Behringer, R., Oron, A., 2007. Marangoni convection in binary mixtures. Phys. Rev. E 23, 016306.

[58] Zhang, J., Oron, A., Behringer, R., 2011. Novel pattern forming states for Marangoni convection in volatile binary liquids. Phys. Fluids 23, 072102.

[59] Zhang, K. J., Briggs, M. E., Gammon, R. W., Sengers, J. V., Douglas, J. F., 1999. Thermal and mass diffusion in a semidilute good solvent-polymer solution. J. Chem. Phys. 111 (5), 2270–2282.

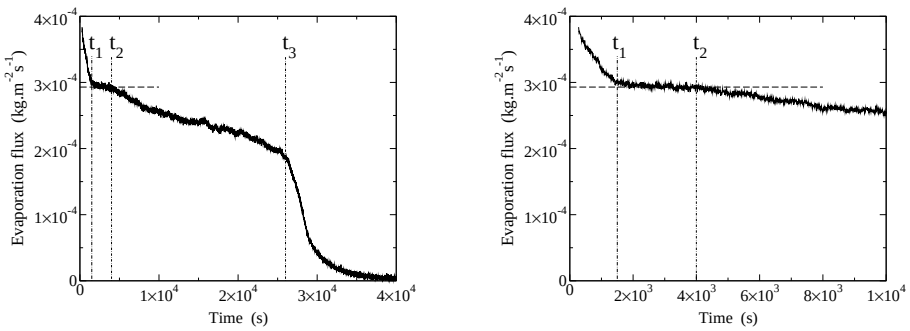


Figure C.1: Experimental evaporation flux as a function of time (experimental conditions corresponding to test case 2 in table 1). The right figure is a focus on the initial stages. Times $t_1$, $t_2$, $t_3$ (vertical dashed-dotted lines) separate the different regimes. The horizontal dashed line represents the plateau for $t_1 \lesssim t \lesssim t_2$.

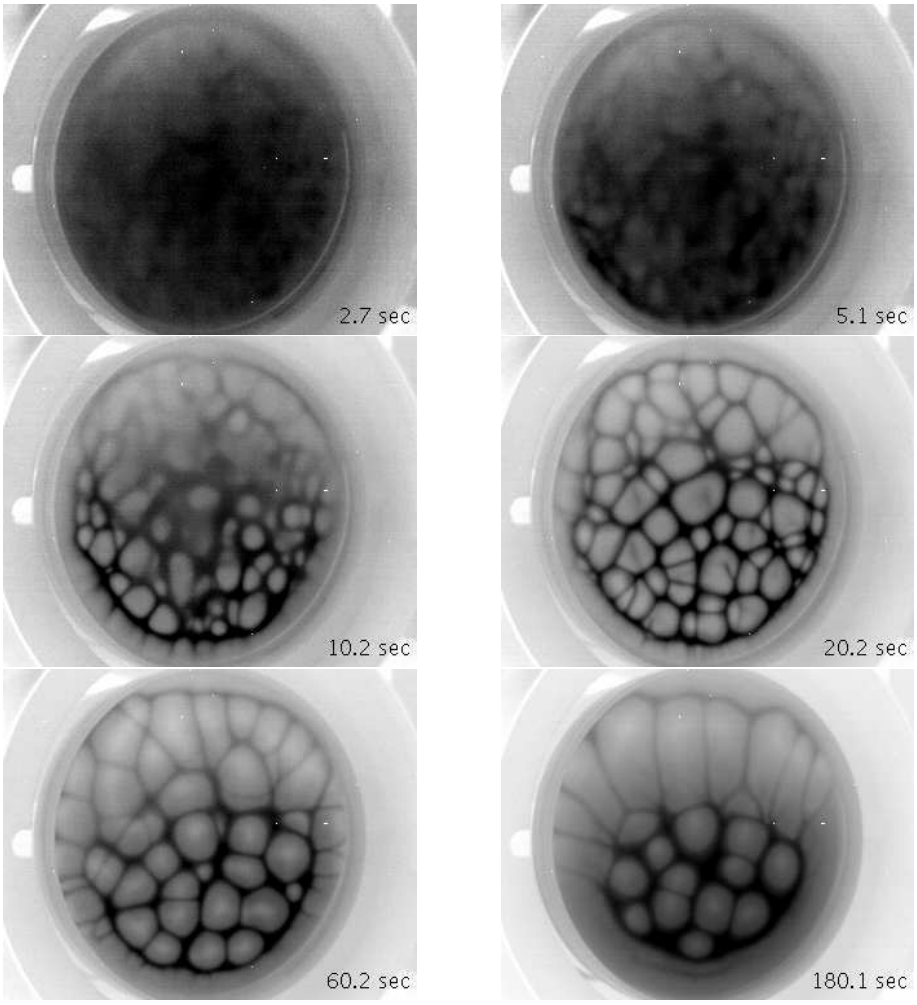


Figure C.2: Formation of thermal convection cells observed by infrared camera (experimental conditions of test case 2 in table 1). The dimensional time corresponding to each image is indicated in the lower right corner.

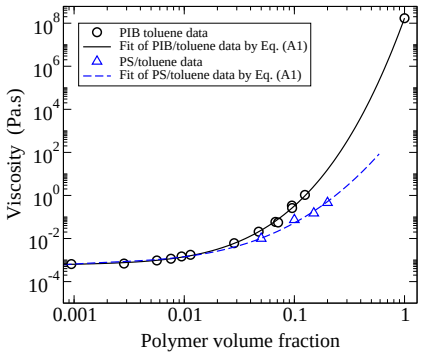


Figure C.3: Variation of viscosity with polymer volume fraction $\varphi_p$ (data from Gorand et al. [17], Mark [25] for PIB/toluene, Bassou and Rharbi [2] for PS/toluene).

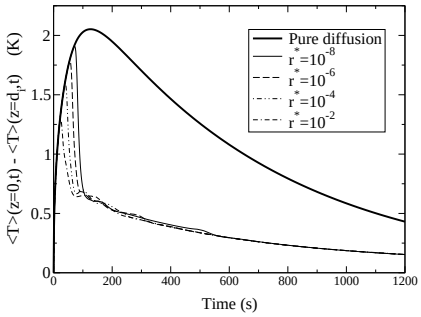


Figure C.4: Thermal model for test case 2 in table 1: difference $< T(z=0,t) > - < T(z=d,t) >$ of the horizontal mean temperatures as a function of time. The thick line represents the pure diffusive case (obtained by setting $\alpha_{th} = 0$ and $\gamma_{th} = 0$ i.e. $Ra_{th} = Ma_{th} = 0$), other lines represent convective cases for different initial amplitudes $r^*$ for temperature perturbations.

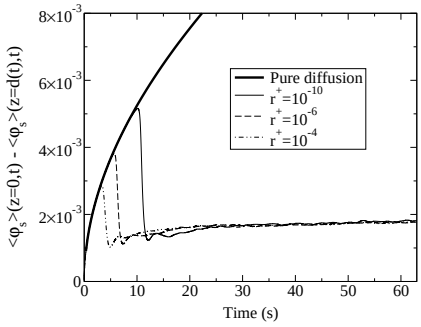


Figure C.5: Solutal model for test case 2 in table 1: difference $< \varphi_s(z=0,t) > - < \varphi_s(z=d(t),t) >$ of horizontal mean solvent volume fractions as a function of time. The thick line represents the pure diffusive case (obtained by setting $\alpha_{sol} = 0$ and $\gamma_{sol} = 0$ i.e. $Ra_{sol} = Ma_{sol} = 0$), other lines represent convective cases for different initial amplitudes $r^+$ for solvent volume fraction perturbations.

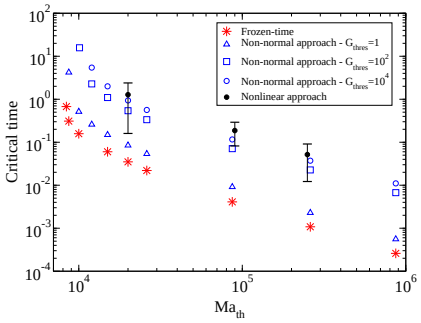


Figure C.6: Times $t^*_{on}$ of convection onset obtained as a function of Marangoni numbers $Ma_{th}$ using different approaches: $t^{*(fr)}_{on}$ given by the frozen-time approach ; $t^{*(nn)}_{on}$ given by the non-normal approach with $E_T$ norm and different thresholds $G_{thres}$ ; $t^{*(nl)}_{on}$ given by the nonlinear approach for different perturbation amplitudes ($10^{-7} \leq r^* \leq 10^{-2}$ for $Ma_{th} = 2 \times 10^4$, $10^{-9} \leq r^* \leq 10^{-4}$ for $Ma_{th} = 9 \times 10^4$ and $Ma_{th} = 2.5 \times 10^5$). The other dimensionless parameters are such that $Ra_{th} = 0$, $Bi = 0.01$. For non-normal and frozen-time methods, Prandtl number is set to $Pr = \infty$, for the nonlinear approach, it is set to $Pr = 100$.

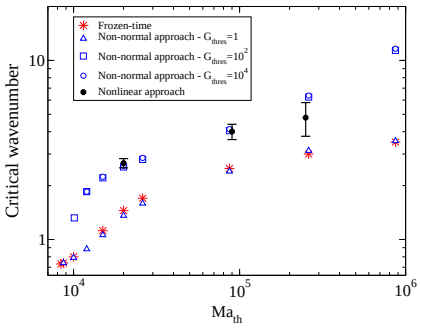


Figure C.7: Wavenumber $k^*_{on}$ at onset obtained as a function of Marangoni number $Ma_{th}$ using different approaches. Same conditions than figure C.6. $k^{*(fr)}_{on}$ is given by the frozen-time approach, $k^{*(nn)}_{on}$ by the non-normal approach with different thresholds $G_{thres}$ ; $k^{*(nl)}_{on}$ by the nonlinear approach.

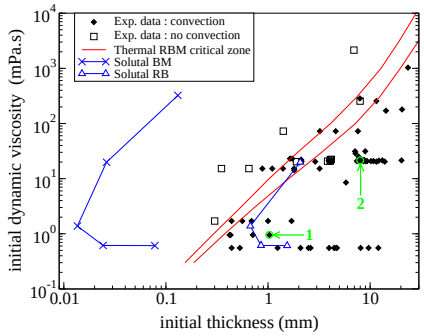


Figure C.8: Stability diagram for PIB/toluene solution (room temperature, $v_{ev} \simeq 0.3\ \mu\text{m.s}^{-1}$, $\Delta T_{st} \simeq 5$ K, $H_{th} \simeq 28\ \text{W.m}^{-2}\text{.K}^{-1}$). The critical zone of the thermal Rayleigh-Bénard-Marangoni problem corresponds to the extreme boundaries obtained by the non-normal method formed by curves $G_{thres} = 1$ or $G_{thres} = 100$ using $E_V$ or $E_T$ norms (see Doumenc et al. [12]). The critical conditions of the solutal Bénard-Marangoni problem and the solutal Rayleigh-Bénard problem have been obtained by the nonlinear approach with $r^+ = 10^{-6}/\Delta\varphi$ (see Trouette et al. [48]). Changing $r^+$ by $\pm$ 2 decades results in a maximum variation of the critical thickness of the order of 30 % (not shown on the plot). Experimental test cases 1 and 2 are indicated by green circles and arrows.

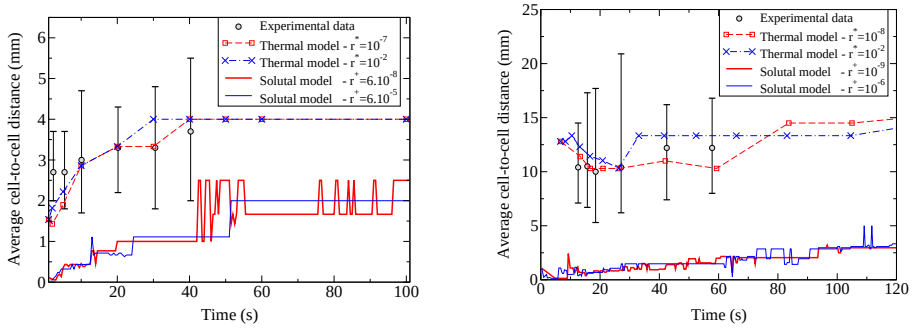


Figure C.9: Time evolution of the average cell-to-cell distance for thermal model, solutal model, and experiments. Left: Test case 1, Right: Test case 2. Error bars in experimental results reflect the size dispersion of the cells.

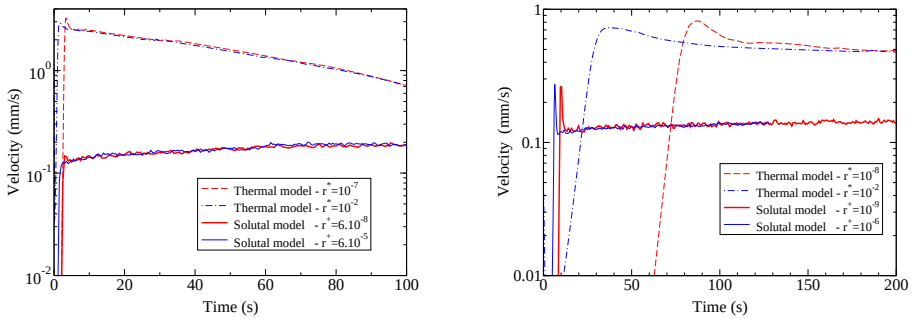


Figure C.10: Time evolution of free surface velocity for thermal and solutal models ($L_2$ norm). Left: Test case 1, Right: Test case 2.

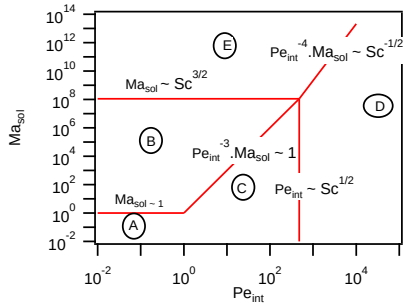


Figure C.11: Solutal model: quasi-steady regime in the BM configuration. Domains derived from the scaling analysis (the figure is drawn for $Sc = 2.3 \times 10^5$).

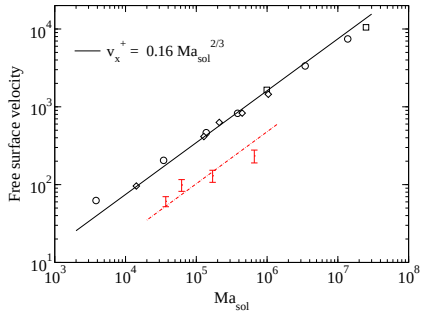


Figure C.12: Solutal Bénard-Marangoni problem: average dimensionless velocity at the free surface. Black open symbols: L2 norm from numerical simulations (○: PIB/toluene, $\varphi_{pi} = 0.047$, $A = 5$, constant viscosity ; □: PIB/toluene, $A = 10$, variable viscosity ; ◇: PS/toluene, $A = 30$, variable viscosity ; Straight line: scaling law (B domain, prefactor fitted over numerical simulations) ; Error bars: experimental data from Bassou and Rharbi [2].